Alma Mater Studiorum - Università di Bologna

DOTTORATO DI RICERCA IN ASTRONOMIA

Ciclo XXI

Settore scientifico di afferenza: Area 02 - Scienze Fisiche

FIS/05 Astronomia e Astrofisica

MCAO for Extremely Large Telescopes: the cases of LBT and E-ELT

Presentata da: LAURA SCHREIBER

Coordinatore Dottorato

Ch.mo Prof. Lauro Moscardini

Relatore

Ch.mo Prof. Bruno Marano

Dott. Emiliano Diolaiti

Esame finale anno 2009

Ad Antonio

Contents

Acronyms

AO	Adaptive Optics
CW	Continuous Wave
DM	Deformable Mirror
EAO	Extreme Adaptive Optics
E-ELT	European Extremely Large Telescope
ESO	European Southern Observatory
FDR	Final Design Review
FoV	Field of View
FWHM	Full Width Half Maximum
GS	Guide Star
GWS	Ground Layer Wavefront Sensor
IFU	Integral Field Unit
IR	Infrared
K-L	Karhunen-Loeve
LBT	Large Binocular Telescope
LGS	Laser Guide Star
LN	Linc-Nirvana
MAD	Multi Conjugate Adaptive Optics Demonstrator
MCAO	Multi Conjugate Adaptive Optics
MHWS	Mid-High Wavefront Sensor
MOAO	Multi-Object Adaptive Optics
MPIA	Max-Planck-Institut fur Astronomie
NGS	Natural Guide Star
OPD	Optical Path Difference
RMS	Root Mean Square
RON	Read Out Noise
PSF	Point Spread Function
PV	Peack to Valley
SH	Shack Hartmann
SR	Strehl Ratio
SE	Star Enlarger
TNT	Thirty Meter Telescope
VLT	Very Large Telescope
WF	Wavefront
WFE	Wavefront Error
WFS	Wavefront Sensor

Introduction

Over the last years increasing interest has been given to the design of ground-based telescopes with very large diameters (up to 40 m). The advantages that such signal collecting surfaces offer to the progress of astrophysics research are so relevant to justify such an effort. In an ideal diffraction limited telescope the signal-to-noise ratio is proportional to the fourth power of the telescope diameter and the angular resolution depends linearly on the telescope diameter too. In this context the use of AO is crucial to approach this full potential. However single reference AO presents many limiting factors due to the lack of suitable reference stars and to the vertical extension of the atmospheric turbulence structure. The main consequences are the reduction of sky coverage (fraction of the sky where an efficient correction can be achieved) and the small corrected field. The usage of LGSs as 'mobile' reference sources partially solves only the sky coverage issue. A very promising solution is given by MCAO, correcting more than one turbulent layer by means of many DMs. The feasibility of the MCAO techniques has been demonstrated on sky in March 2007 at VLT with MAD.

Several MCAO systems are under study to improve the angular resolution of the current and of the future generation large ground-based telescopes (diameters in the 8-40 m range). The subject of this PhD Thesis is embedded in this context. Two MCAO systems, in different realization phases, are addressed in this Thesis: NIRVANA, the 'double' MCAO system designed for one of the interferometric instruments of LBT, is in the integration and testing phase; MAORY, the future E-ELT MCAO module, is under preliminary study. These two systems takle the sky coverage problem in two different ways.

The layer oriented approach of NIRVANA, coupled with multi-pyramids wavefront sensors, takes advantage of the optical co-addition of the signal coming from up to 12 NGS in a annular 2' to 6' technical FoV and up to 8 in the central 2' FoV. Summing the light coming from many natural sources

permits to increase the limiting magnitude of the single NGS and to improve considerably the sky coverage. One of the two Wavefront Sensors for the mid-high altitude atmosphere analysis has been integrated and tested as a stand-alone unit in the laboratory at INAF-Osservatorio Astronomico di Bologna and afterwards delivered to the MPIA laboratories in Heidelberg, where was integrated and aligned to the post-focal optical relay of one LINC-NIRVANA arm. A number of tests were performed in order to characterize and optimize the system functionalities and performance. A report about this work is presented in Chapter 2.

In the MAORY case, to ensure correction uniformity and sky coverage, the LGS-based approach is the current baseline. However, since the Sodium layer is approximately 10 km thick, the artificial reference source looks elongated, especially when observed from the edge of a large aperture. On a 30-40 m class telescope, for instance, the maximum elongation θ_{elo} varies between few arcsec and 10 arcsec, depending on the actual telescope diameter, on the Sodium layer properties and on the laser launcher position. The centroiding error in a Shack-Hartmann WFS increases proportionally to the elongation (in a photon noise dominated regime), strongly limiting the performance. To compensate for this effect a straightforward solution is to increase the laser power, i.e. to increase the number of detected photons per subaperture. The scope of Chapter 3 is twofold: an analysis of the performance of three different algorithms (Weighted Center of Gravity, Correlation and Quad-cell) for the instantaneous LGS image position measurement in presence of elongated spots and the determination of the required number of photons to achieve a certain average wavefront error over the telescope aperture. An alternative optical solution to the spot elongation problem is proposed in Section 3.4. Starting from the considerations presented in Chapter 3, a first order analysis of the LGS WFS for MAORY (number of subapertures, number of detected photons per subaperture, RON, focal plane sampling, subaperture FoV) is the subject of Chapter 4. An LGS WFS laboratory prototype was designed to reproduce the relevant aspects of an LGS SH WFS for the E-ELT and to evaluate the performance of different centroid algorithms in presence of elongated spots as investigated numerically and analytically in Chapter 3. This prototype permits to simulate realistic Sodium profiles. A full testing plan for the prototype is set in Chapter 4.

Chapter 1

The Giant Telescopes epoch

1.1 Multi-Conjugate Adaptive Optics

The development of AO techniques (Babcock, 1953) has permitted to enhance the angular resolution of large ground based telescopes by correcting in real time the aberrations induced by the atmosphere. The signal coming from a reference source (usually a star) is used to measure the wavefront aberrations and a DM corrects them to produce a diffraction-limited (FWHM $\sim \lambda$/D), rather than seeing-limited (FWHM $\sim$ 0.5 - 1.0 arcsec) image of the science target (see Figure 1.1). Since the atmospheric turbulence structure presents a vertical extension, light from different directions experiences different distortions (see Figure 1.2). In other words, although atmospheric refractive-

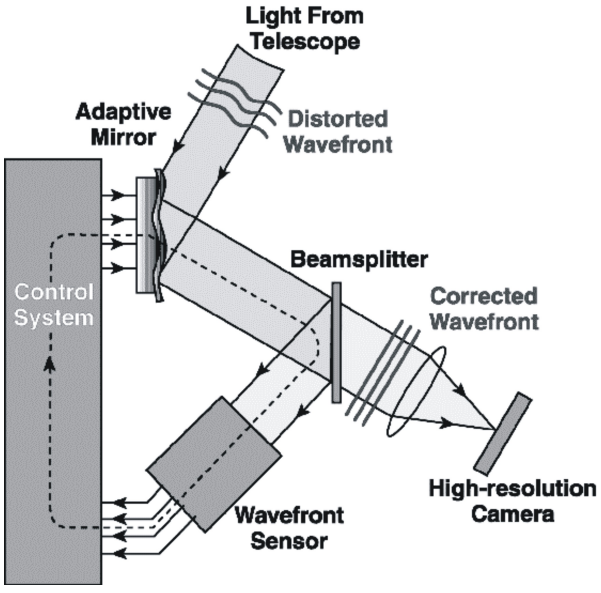

Figure 1.1: Scheme of an adaptive optics system.

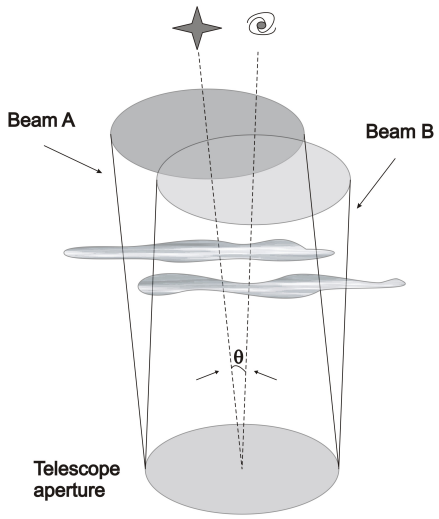

Figure 1.2: Illustration of angular anisoplanatism. The wavefront measured within Beam A (the guide star) is not valid for Beam B (the science object) since the two volumes of atmosphere are different. Thus, a correction which is perfect for Beam A will not be perfect for Beam B.

index inhomogeneities form a three dimensional spatial random process, an AO system applies only a two-dimensional correction adapting the surface of the DM. The correlation between the surface of the DM and the cumulative phase distortion along other propagation directions decreases rapidly with the offset angle between the reference and the scientific object direction. This effect is commonly referred to as angular anisoplanatism (Roddier et al., 1993). In order to achieve an acceptable correction on the science object it is therefore necessary to select a guide star within the isoplanatic angle of the science target (few arcsec in the visible and few tens of arcsec in the IR). A first evident consequence of the anisoplanatism is the small corrected FoV. To provide a sufficient signal-to-noise ratio for the WFS, the guide star has to be also very bright, i.e. at least 15th magnitude for a diffraction limited image at 1.65 μm (Rigaut et al., 1998). These two requests, i.e. GS bright and close to the object, severely limit the fraction of the sky where an efficient correction can be achieved (sky coverage, defined in percentage of sky), and, for near-IR wavelengths, it is few percent (Beckers, 1993). In this context the potential power of LGS AO, proposed by Foy & Labeyrie (1985), is clear. The basic idea is to generate a bright GS in the upper atmosphere by means of a laser. This smart alternative, however, does not solve another big issue of classical AO: even within the immediate neighborhood of a GS, natural or not, the

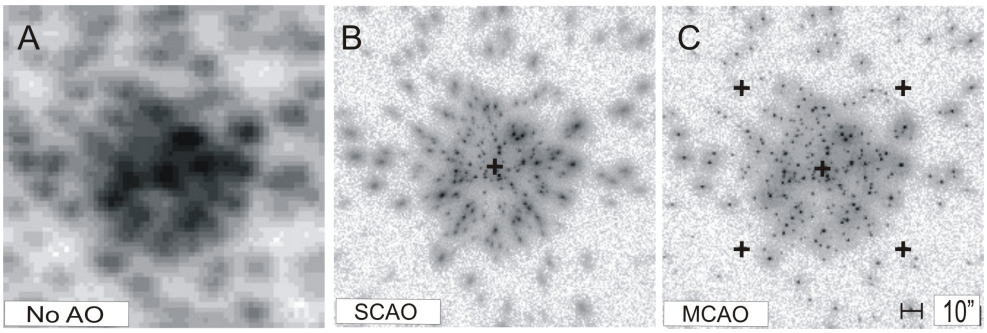

Figure 1.3: Imaging improvement by means of adaptive optics technique. A: blurred seeing limited image: the seeing is 0.7" at 550 nm; B: the application of AO allows the compensation for the image degradation in a small field around the GS (black cross); C: effect on the image of the MCAO correction using more than one reference star (5 black crosses). (Rigaut, Ellerbroeck and Flicker, 2000).

performance of AO is not uniform, producing a variation of the PSF across the FoV (Simon et al., 1999).

MCAO is a technique described for the first time by Beckers (1989) to overcome these limitations and obtain a more uniform correction over a larger field (Ellerbroek & Rigaut, 2000). In MCAO multiple mirrors correct different planes in the atmosphere, in principle producing uniform compensation over a much larger FoV (see Figures 1.3 and 1.5). To calculate the three dimensional distortion due to turbulence, and to command each mirror correctly, requires optical distortion measurements from multiple guide stars (either natural or artificial), each of which provides a measurement of the turbulence in a different direction. Two different MCAO approaches have been described (see Figure 1.4): Star Oriented or tomographic MCAO (Foy & Labeyrie, 1985 and Ragazzoni et al., 1999) and Layer Oriented MCAO (Ragazzoni et al., 2000). Both methods correct at multiple heights in the atmosphere using multiple DMs and multiple WFSs. Tomographic MCAO uses one WFS per guide star (Figure 1.4 left panel) and converts numerically the linear projections of the cumulative phase distortion along the guide stars directions into the original three dimensional profile. In a Layer Oriented system, the WFSs are not coupled to the GSs, but are conjugated with specific layers in the atmosphere. The DMs are conjugated with the same layers as the WFSs and each of them applies a correction proportional to what the corresponding WFS measures, optically combining the light from the GSs.

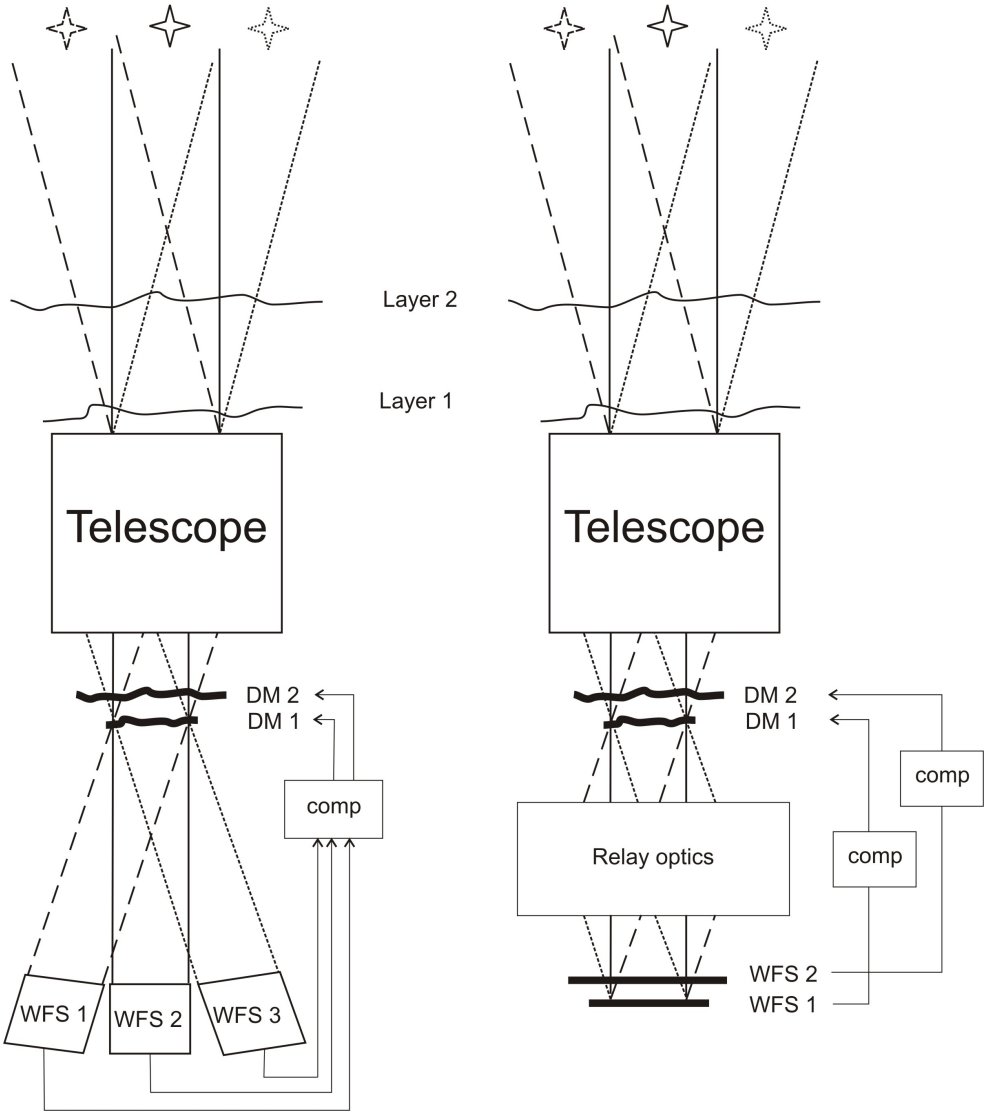

Figure 1.4: Schemes of two multi-conjugate adaptive optics approaches: star oriented mode (left panel) and Layer Oriented mode (right panel).

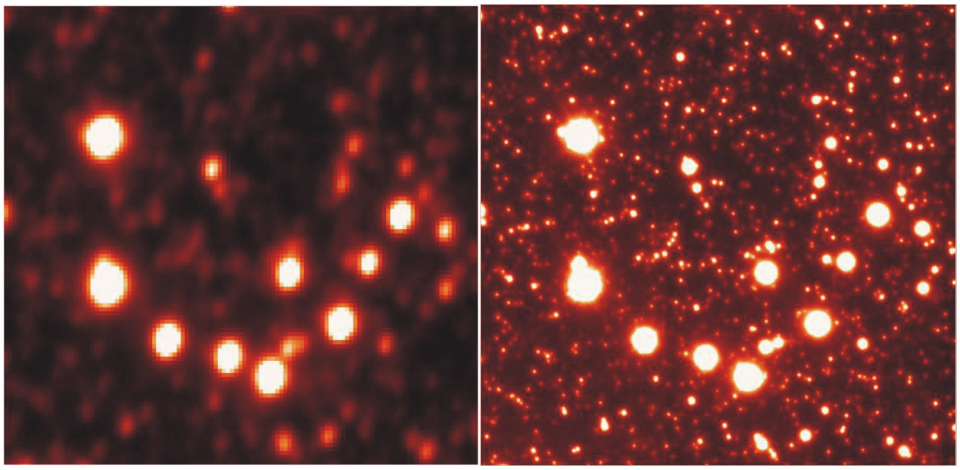

Figure 1.5: MAD at the VLT. Comparison between a natural seeing (0.5"), K band image of the core of the globular cluster ω Cen with ISAAC (left) and a MAD image in the same filter obtained while the seeing was 0.7" (right). The image is a 15" $\times$ 15" cutout from the $2' \times 2'$ corrected FoV, and has a very homogenous image quality (Strehl $> 20\%$ everywhere). (Gilmozzi & Spyromilio, 2008).

1.2 The Large Binocular Telescope

The LBT Project is a collaboration between institutions in USA, Germany and Italy. The telescope, situated on Mt. Graham in southeastern Arizona,

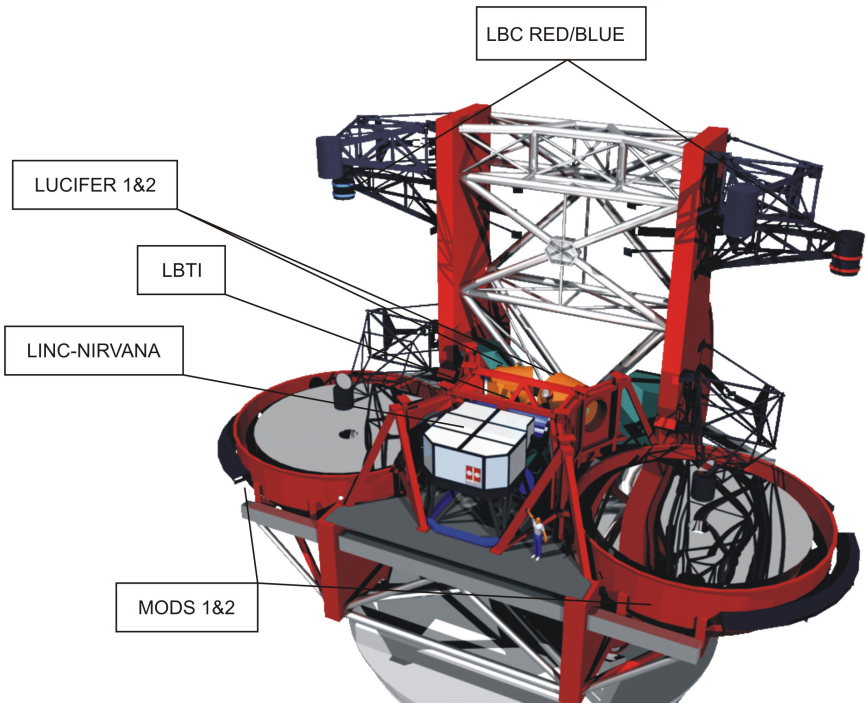

Figure 1.6: The Large Binocular Telescope.

uses two 8.4 meter diameter primary mirrors mounted side-by-side to produce a collecting area equivalent to an 11.8 meter circular aperture. This makes the LBT the most powerful single mount telescope in the world in terms of light collection capability. A unique feature of LBT is that the light from the two primary mirrors can be combined optically in the center of the telescope re-imaging the two folded Gregorian focal planes to three central locations, giving the possibility to reach the diffraction-limited resolution of a 22.65 meter telescope. For this purpose the interferometric instruments of LBT (LINC-NIRVANA and LBTI) make use of adaptive optics. The main wavefront correctors are the two adaptive secondaries mirrors of a Gregorian design (concave ellipsoidal mirrors), undersized to provide a low thermal background focal plane. LN will implement an additional wavefront corrector conjugate at a higher layer after the Gregorian focus. The LBT has 10 focal stations to host single-channel and interferometric instruments (see Figure 1.6). The

single channel instruments are replicated for the two channels and are: two seeing limited cameras (LBC, prime focus stations), two optical Multi-Object spectrographs (MODS, direct Gregorian focus stations behind the primary mirrors), a high-resolution echelle spectrograph with two polarimeters (PEPSI, again direct Gregorian focus stations) and two near-IR imagers - spectrographs for both seeing limited and diffraction limited operations (LUCIFER, bended Gregorian focus stations). Two interferometers, LN for Fizeau interferometry and and LBTI for nulling interferometry, are between the two mirrors in order to combine the bended Gregorian beams.

1.2.1 LINC-NIRVANA Overview

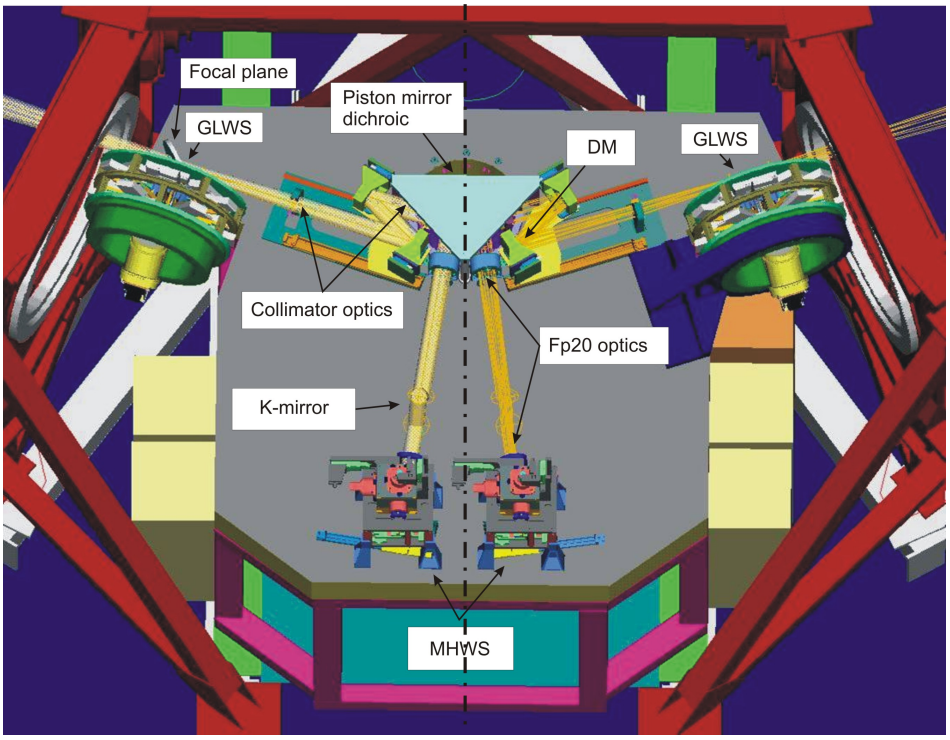

Figure 1.7: LN overview. It will be mounted between the two primary mirrors on the same mount of the telescope, enabling the instrument to move rigidly with all the telescope structure. The dotted-dashed line across the Figure underline the symmetry of the instrument design.

The peculiar structure of the LBT is characterized by two 8.4 meter primary mirrors on a single common mount. This 'double telescope' offers different configuration choices. One of these allows to combine the beams coming from the two collecting surfaces in a Fizeau interferometric mode, to

make the beams interfere directly on the image plane. LN (Herbst et al., 2003), positioned between the two primary mirrors, on the same mount of the telescope, is the instrument designed for this purpose (see Figure 1.7). Before being combined, the two beams are corrected from the distortions due to the atmospheric turbulence effects on FoV of 2 arcmin. A double MCAO (Ragazzoni et al., 2003) system based on the Layer Oriented approach (Ragazzoni et al., 2002) is conceived to correct independently the wavefronts coming from the two sides by means of two multi-pyramids (Ragazzoni, 1996) WFS driving two DMs conjugated to different altitudes. Twelve reference stars (maximum) in an annular field of view between 2 and 6 arcmin will feed the Ground layer WFS (GWS), driving the deformable secondary mirrors of the telescope. The central 2 arcmin beam passes through the collimator optics which include two groups of three lenses each and the deformable mirror driven by the Mid-High layer Wavefront Sensor (MHWS). This mirror in the post-focal relay, will be mounted on a rail line to permit a range of conjugations between 4 and 15 km. The system is designed to allow an improvement in the future with a third deformable mirror dedicated to the medium atmosphere's layers (4 - 8 km). A piston mirror compensates in real time the OPD between the beams coming from the two telescopes and folds them into vertical direction where a dichroic splits visible and IR light: the latter is transmitted into a cryostat where interference takes place on the scientific camera, the former is reflected to the MHWS. Collimated visible light feeds an optical system, called FP20 camera, consisting of four lenses and a K-mirror to compensate the field rotation, ensuring a telecentric f/20 beam at the focal plane at the entrance of the MWHS. A more detailed description of all these components (collimator, DM, FP20 optics, K-mirror) forming the so called 'warm optics' and of the MHWS is reported in Chapter 2.

1.3 The European Extremely Large Telescope

The EELT (Gilmozzi & Spyromilio, 2008) is a project led by ESO with a scheduled first light in 2017. With its 42 meters diameter primary mirror, made of 984 1.45 m hexagonal segments for a total of 1300 meters square collecting area, it will be the bigger ground-based telescope ever built. The E-ELT size has been determined by a good compromise between the science requirements, traded off with the technical feasibility, and the available budget.

The optical design is based on a 5 mirrors design: three surfaces with optical power (M1 = 42 m, M2 = 6 m convex and M3 = 4 m) and two flat mirrors (M4 = 2.6 m and M5 = 2.7 m) that bend the beam in the direction of one of the two Nasmyth platforms. The telescope provides also a Coudé focus for large instrumentation and two gravity invariant focal stations (one for each Nasmyth platform). M4 and M5 have adaptive and field stabilization roles in the optical train of the telescope. The image quality of the telescope is diffraction limited over the full field of view of 10 arcmin.

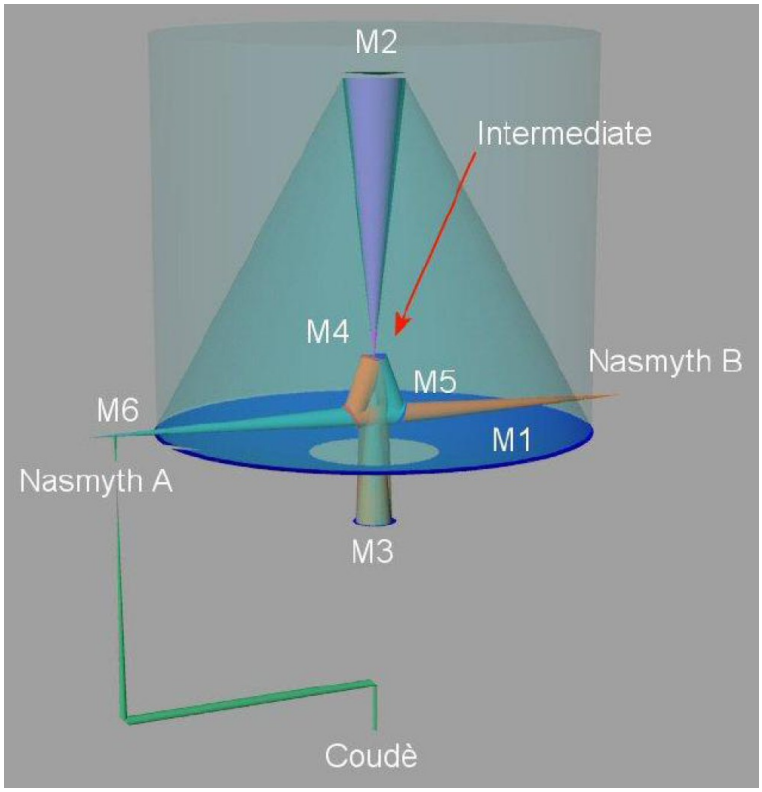

Figure 1.8: E-ELT optical scheme and focal stations.

A phase A design study is underway for a number of instrument concepts. The instrumentation complement has been matched to the science cases. Under study are (see EELT Website): an high spectral resolution ultra stable optical spectrograph (CODEX), a planet imager and spectrograph with EAO (EPICS), a wide field multi IFU near-IR spectrograph with MOAO (EAGLE), a single field wide band spectrograph (HARMONI), a mid-IR imager and spectrograph with AO (METIS), a diffraction-limited near-IR camera (MICADO), a wide field visual multi-object spectrograph (OPTIMOS)

and a high spectral resolution near-IR spectrograph (SIMPLE). Also two post-focal AO modules are under study: a laser tomography AO Module (ATLAS) and a MCAO module (MAORY).

1.3.1 MAORY Overview

The post-focal MCAO module for the European Extremely Large Telescope, MAORY (Diolaiti et al., 2008), providing a corrected field up to 2 arcmin over the baseline wavelength range 0.8 - 2.4 μm, will be suitable to feed high angular resolution imaging cameras and spectrographs. To ensure correction uniformity and sky coverage, the LGS-based approach is the current baseline. The suitable number of guide stars (6) and post-focal deformable mirrors (2 DM conjugated to 4 and 12.7 km see Figure 1.9) has been evaluated optimizing the system performance by means of a Fourier code (Conan et al., 2008). It has to be taken in mind that ground-layer correction and field stabilization are provided by the adaptive telescope, respectively through mirrors M4 and M5 (see Section 1.3). From the wavefront sensing point of view, the MCAO module is characterized by a multiple Sodium LGS wavefront sensor for the high-order sensing and a multiple NGS wavefront sensor, to measure the low-order modes, that determines the final sky coverage.

The preliminary expected performance, including all the error sources, is presented in Table 1.1 for the 2' FoV and considering two different seeing conditions. The performance is reported in terms of Strehl Ratio, defined as the ratio of the observed peak intensity at the detection plane of an imaging system from a point source compared to the theoretical maximum peak intensity of a perfect imaging system working at the diffraction limit.

Seeing	**K band**	**H band**	**J band**	**Y band**	**I band**
0.65"	0.51	0.32	0.15	0.06	0.03
0.85"	0.41	0.23	0.09	0.04	0.01

Table 1.1: SR average and RMS over a 2' FoV considering two different seeing conditions. Starting from the left, the considered bands are centered in: λ=2.2 μm, λ=1.65 μm, λ=1.25 μm, λ=1.1 μm and λ=0.9 μm. The SR RMS over the 2' FoV is $\leq$ 0.13.

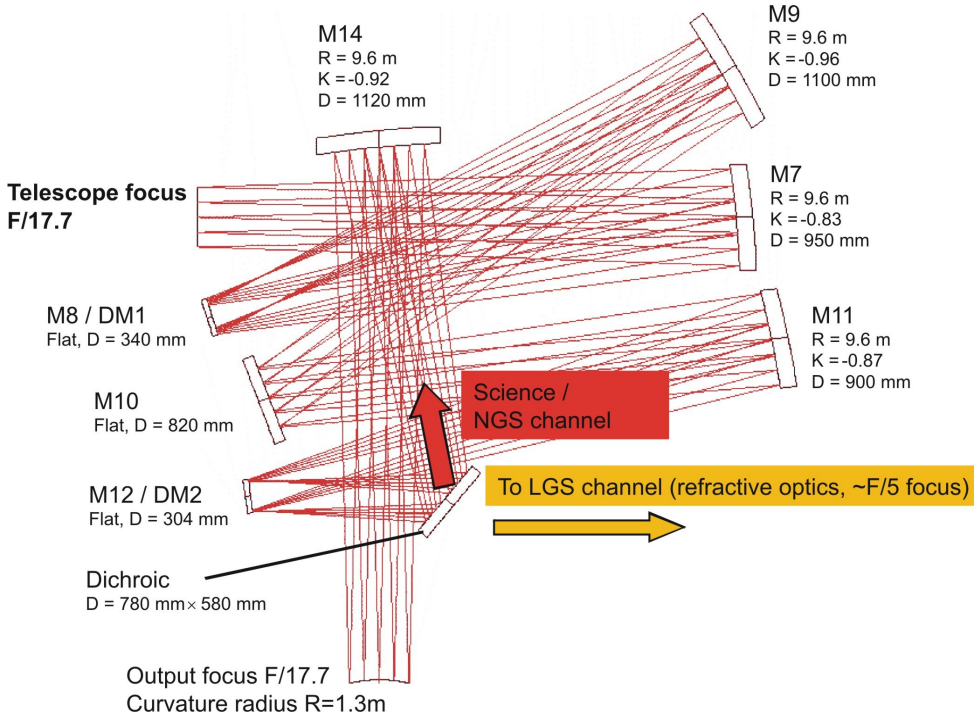

Figure 1.9: MAORY preliminary optical design. Two post-focal flat deformable mirrors correct the hight-altitude layers (DM1 and DM2) and a dichroic splits the light between the LGS wavefront sensor channel and the science-NGS wavefront sensor channel. (Courtesy of Emiliano Diolaiti, INAF, Osservatorio Astronomico di Bologna)

1.4 Other MCAO systems

The MCAO technique feasibility was demonstrated with **MAD** (VLT), the ESO Multi conjugate Adaptive optics Demonstrator (Viard et al., 2000, Hubin et al., 2002). Since MAD is a demonstrator, it has been designed in a double mode configuration: Star Oriented multi Shack-Hartmann wavefront sensor (Marchetti et al., 2006), that benefits of maximum 3 natural guide stars, and Layer Oriented multi–pyramids (Ragazzoni et al., 2000) wavefront sensor with the possibility to co-add the light coming from maximum 8 natural guide stars. The adaptive system is completed by two deformable mirrors conjugated to 0 and 8.5 km. The first MCAO loop on the sky was closed on the open cluster NGC 3293 the night of 25 March 2007 in star oriented mode. After routine checks on the closed loop stability, the telescope was pointed to Omega Centauri (Bono et al., 2009).

The MCAO system designed for the **Gemini-South** 8 meter telescope

(Ellerbroek et al., 2003) will provide uniform atmospheric turbulence compensation at near-IR wavelengths over a 1 square arcmin field-of-view. Even if the SR degrades outside this field, the total usable field corresponds to 2 arcmin field in H and K bands, and approximately 1.5 arcmin at J. The design includes three deformable mirrors optically conjugated to ranges of 0, 4.5, and 9.0 kilometers, five 10-Watt-class sodium LGSs (one 50 Watt CW laser splitted in 5 beams, 1 on axis and 4 arranged on a constellation 30" wide) projected from a laser launch telescope located behind the Gemini secondary mirror, five Shack-Hartmann LGS wavefront sensors of order 16 $\times$ 16 subapertures, and three tip/tilt NGS wavefront sensors.

The TMT (funded by USA and Canada) will also have a facility MCAO system: **NFIRAOS** (Herriot et al., 2006). The requirements include 0.8 - 2.5 μm wavelength range across a 30 arcsec diameter output FoV. The reference design for NFIRAOS includes multiple sodium LGSs over a 70 arcsec FoV, and 3 IR tip/tilt/focus/astigmatism NGSs. The beacons on the sky are arranged in a 70 arcsec diameter circle plus a beacon at the center of the pentagon. NFIRAOS uses two deformable mirrors in series conjugated to 0 and 12 km, to correct a 2 arcmin diameter technical field to sharpen near-IR natural guide stars and improve sky coverage. NFIRAOS is also capable of operating in natural guide star mode when laser beacons are not available.

Chapter 2

The NIRVANA post-focal relay integration

As described in the previous chapter, LINC-NIRVANA is an infrared camera working in Fizeau interferometric mode. The beams coming from the two primary mirrors of the Large Binocular Telescope (LBT) are corrected for the effects of the atmospheric turbulence by two (identical) MCAO systems. The corrected field of view is 2 arcmin diameter. One single arm MCAO system includes two WFSs, driving two DMs: one Ground Layer Wavefront Sensor (GLW) that drives the LBT secondary mirror, and one Mid-High layer Wavefront Sensor (MHWS). The first of the two MHWS was integrated and tested as a stand-alone unit in the laboratory at INAF-Osservatorio Astronomico di Bologna, where the telescope was simulated by means of a simple afocal system illuminated by a set of optical fibers. Then the module was delivered to the MPIA laboratories in Heidelberg, where it was integrated and aligned to the post-focal optical relay of one LINC-NIRVANA (LN) arm (Schreiber et al., 2008a). Scope of this chapter is to describe and summarize the work done in Bologna and in Heidelberg in the framework of this PhD Thesis.

2.1 The post-focal Relay

This Section describes the post-focal relay optical components of only one arm of the telescope. Since LN is fed by both the telescopes forming LBT, all the components exist in double copy. The warm fore-optics (Figure 2.1) consist of the following sub-systems:

- collimator optics: two groups of lenses that collimate the f/15 light

from the telescope focus. Between the two groups, where the DM is located, the beam diameter for all fields is constant (constant envelope, see Figure 2.2). The two sets of collimator optics must have the same focal length to generate pupil images with the same diameter, necessary condition to meet the requirement on the pupils homotheticity (the diameter and the separation of the two pupils formed by the two collimators must be identical to the ratio of telescope entrance pupil diameter to telescopes separation). Pupils homotheticity is a fundamental condition for the interferometric operations of the instrument.

- DM: can be conjugated in a range of altitudes between 4 and 15 km, where the atmospheric turbulence is concentrated;
- FP20 optic: they generate a F/20 telecentric flat focal plane at the entrance of the WFS;
- motorized K-Mirror: for the compensation of the field rotation.

The F/20 beam is then folded up to the MHWS.

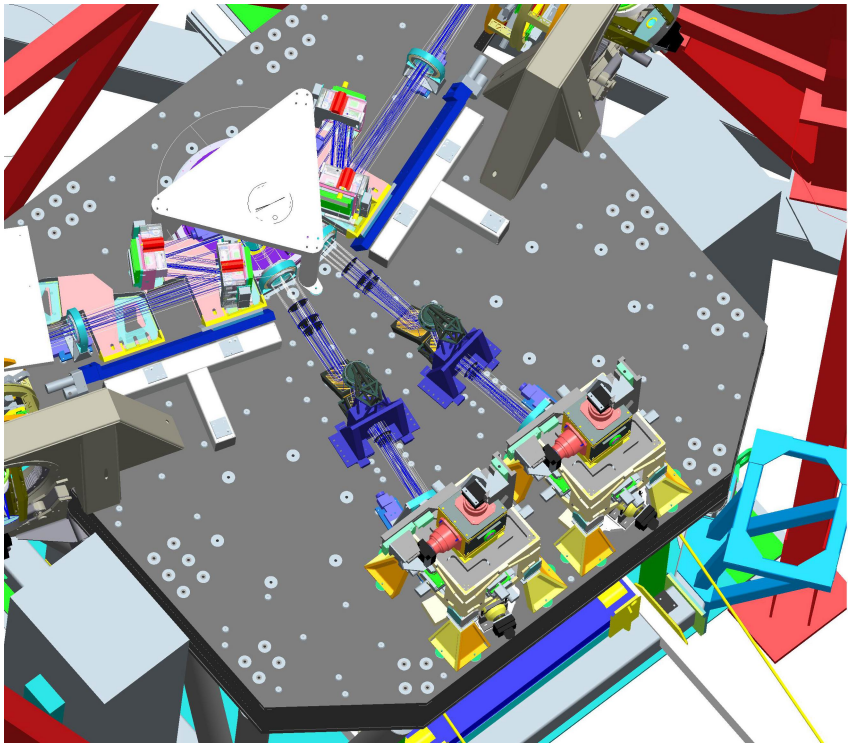

Figure 2.1: LINC-NIRVANA post-focal relay overview.

All the optical elements of the post-focal relay before the MHWS that are not cryogenic are called 'warm optics'. The main requirements of the warm optics are summarized in Table 2.1.

Optical element	**Item**	**Requirement**
Collimator	Input	post-focal beam F/15.27
	Wavelenght range	0.6 μm to 2.4 μm
	Blur of pupil	$\leq$ 0.7 mm
	Intermediate beams for DMs	Constant envelope of $\sim$140 mm
FP20	Input	$\oslash$ 126 mm collimated beam
	Wavelenght range	0.6 μm to 0.9 μm
	Field curvature	Flat
	WFE	$<$ 30 nm
	F/number	F/20 $\pm$ 0.1
	Non telecentricity angle	$<$ 0.014°
K-mirror	Reflectivity	$>$ 96% in the range 0.6-1.0 μm
	Internal optical path	640 mm

Table 2.1: Main requirements of the optical elements of the post-focal relay without the Mid-High wavefront Sensor.

The aim of this section is to give a description of each warm optics component and to report the verification test results performed on them.

2.1.1 Collimator and Deformable Mirror

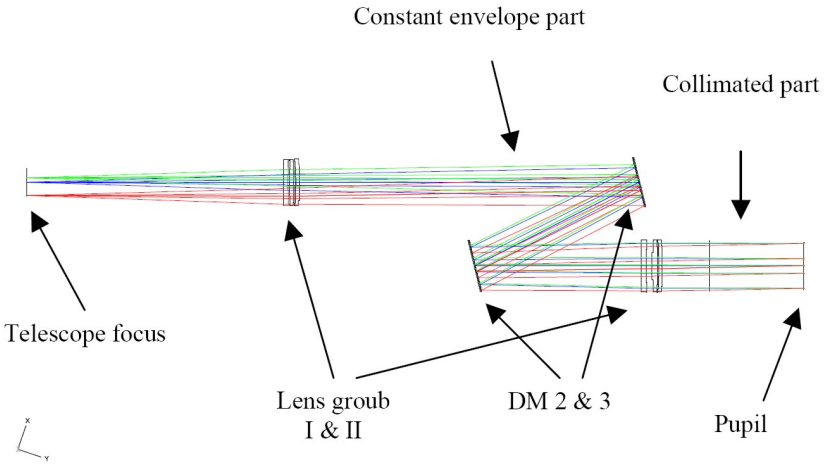

Figure 2.2: Layout of the Collimator optics.

One collimator consists of two separate lens groups, each including three air-spaced lenses on the same mount. Each mount is adjustable in three dimensions. The range is 2 mm in centering tuning and 2° in tilt with an

accuracy respectively of 0.02 mm and 0.0083°. The center of tilt is roughly in the middle between the first and last surface, on the optical axis. The aim of the collimator optics is to convert the F/15.27 beam coming from the telescope in a collimated beam. Between the two lens group the beam forms a constant envelope in order to make use of all the DM actuators at any conjugation altitude. Both aligned collimators were tested (Roth, 2006) and meet the specifications according to Table 2.1.

The DM was manufactured by Xinetics and contains 349 actuators located on a square grid of 21×21 actuators, each made of a piezo-stack and attached to a continuous face-sheet as the reflecting surface. The DM was tested for linearity and hysteresis for different ambient temperatures.

2.1.2 FP20 Optics and K-mirror

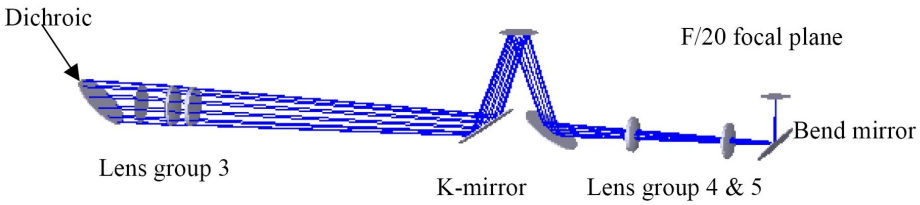

Figure 2.3: Layout of the FP20 optics.

Three groups of lenses, with the same mountings as the collimator lenses, form the FP20 optics (Figure 2.3). Fed by collimated light, they ensure a telecentric F/20 beam over 2 arcmin field of view. The optical quality of the system was tested without the K-Mirror and the distance between the first doublet and the third lens was increased in order to compensate for the K-mirror internal optical path. The collimated beam was generated by a FISBA μLens CDCI 2 Plano Objective with an aperture of 152.4 mm mounted on a FISBA μPhase 2 HR Digital Compact Interferometer coupled with a 126 mm diameter pupil stop. The FISBA Objective was mounted on a tilt platform and on a precision rotation stage. The three groups of lenses were also mounted on two orthogonal 25 mm translation stages for the alignment in centering respect to the optical axis.

The optical system was aligned respect to a laser beam generated by an He-Ne laser source. Starting from the last lens group (the closest to the F/20 focal plane), each group was aligned using the back reflections from

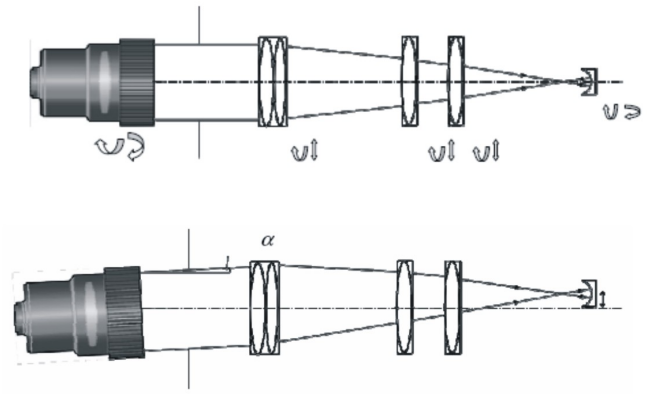

Figure 2.4: Setup for the on-axis (top figure) and off-axis (bottom figure) verification tests.

each lens surface and monitoring the transmitted spots positions on a DVC CCD. The measurement of the residual WFE, i.e. of the optical quality of the system, was performed using the FISBA with the Plano Objective and a Spherical-concave reference surface mounted on two orthogonal stages. To characterize the residual wavefront error over the field of view of 2 arcmin, the measurements were done on-axis and off-axis for five different directions respect to the optical axis (see Figure 2.4). The measurements relative to one of the two FP20 optics set are reported in Table.

Interferometer tilt angle (elevation, azimuth) [degree]	**Mean PV [nm]**	**Mean RMS [nm]**
(0., 0.)	98.66	17.066
(0., -1.)	161.538	24.319
(0., +1.)	146.645	28.509
(+1., 0.)	179.697	30.629
(-1., 0.)	159.219	29.94

Table 2.2: Set number 2 of the FP20 optics wavefront error measurements. These numbers are obtained averaging ten different measurements per each interferometer tilt angle.

According to the values reported in Table 2.1 and 2.2, this set of optics meets the specifications. The test has been repeated for the second set of FP20 optics, but the wavefront error measured was too high (around 70 nm on axis, to be compared with values in Table 2.2) to meet the requirements. The cause of the wavefront degradation was identified in an internal misalignment of the doublet, that was sent back to the company.

A telecentric system has the location of the exit pupil at infinity and so

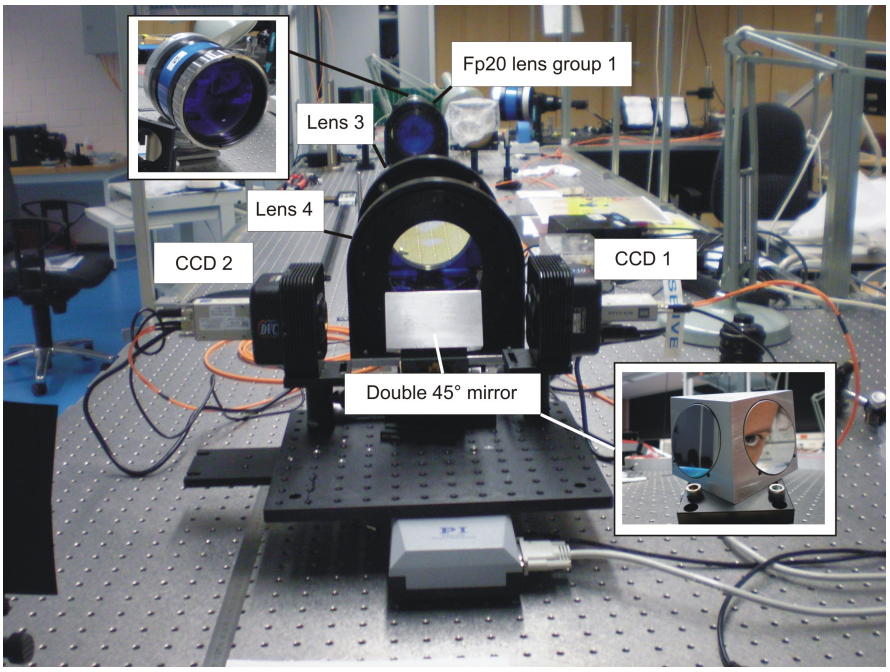

Figure 2.5: Picture of the setup for the FP20 telecentricity verification tests.

the chief rays parallel to the optical axis after the propagation through the system. The non telecentricity angle (see Table 2.1) was measured by means of two DVC CCD mounted on a linear stage parallel to the optical axis in order to trace the direction of the chief rays corresponding to different directions in the sky and measure the angle between them (see Figure 2.6). Since the linear dimension of the field of view at F/20 focal plane is bigger than the CCD, we used a double 45° degrees (also mounted on the linear stage) to bend the beams corresponding to different directions. The direction of the chief rays was traced by measuring the position of the image produced onto the CCD while moving the linear stage along the optical axis. The considered range was 80 mm, images taken every 10 mm.

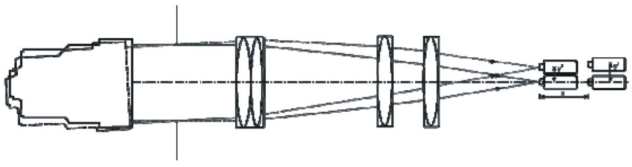

Figure 2.6: Setup for the FP20 telecentricity verification tests.

The centroid coordinates in the eight steps were recorded. After having verified the linear behavior of the coordinates of the image position moving

the linear stage (no appreciable wobbling of the stage), we took, for the non telecentric angle computation, the coordinates of the position of the image in the first and in the last acquired images (i.e. 80 mm far one from the other). The coordinates (in pixel) are reported in Table 2.3.

X_{CCD1}	768.972	772.187
Y_{CCD1}	775.322	765.755
X_{CCD2}	492.549	498.486
Y_{CCD2}	561.63	553.865

Table 2.3: Calculated centroid positions in pixel units for a 8 cm travel range.

If α is the non telecentric angle, $\Delta x = \Delta x(CCD1) - \Delta x(CCD2)$ (the same for y) and Δz is the shift of the linear stage in microns, the following formula gives the non telecentricity angle in radians units:

$$\alpha = p \cdot \frac{\sqrt{\Delta x^2 + \Delta y^2}}{\Delta z} \tag{2.1}$$

where p represents the dimension of one CCD pixel in microns (in this case 1 pixel = 6.45 μm) and Δx and Δy are given in pixels. Putting into Equation (2.1) the measurements reported in Table 2.3, we obtained a non telecentricity angle of 0.015°, slightly out of specifications (0.014°), but accepted because the discrepancy is within the measurement error and therefore negligible.

The K-mirror optical derotator provides the derotation of the field for the MHWS. The two identical units rotate in the same direction during operation, avoiding mutual mechanical interference. The K-mirror has not optical power and consists of three mirrors mounted together in a stiff and stable structure that allows rotation of the assembly around the optical axis of the FP20 camera. There are several adjustment systems for internal alignment and alignment to the post focal relay. The K-mirror verification tests were provided by the manufacturer.

2.2 The Mid-High Wavefront Sensor

The Mid-High layer Wavefront Sensor (Figure 2.7) is a multi-pyramid WFS based on the layer oriented concept. Eight probes move in the field using 16 linear stages, in XY configuration, in order to capture the light of the guide stars. Every probe consists of an afocal system, called "Star Enlarger" (SE), that magnifies the star image individually by increasing the focal ratio,

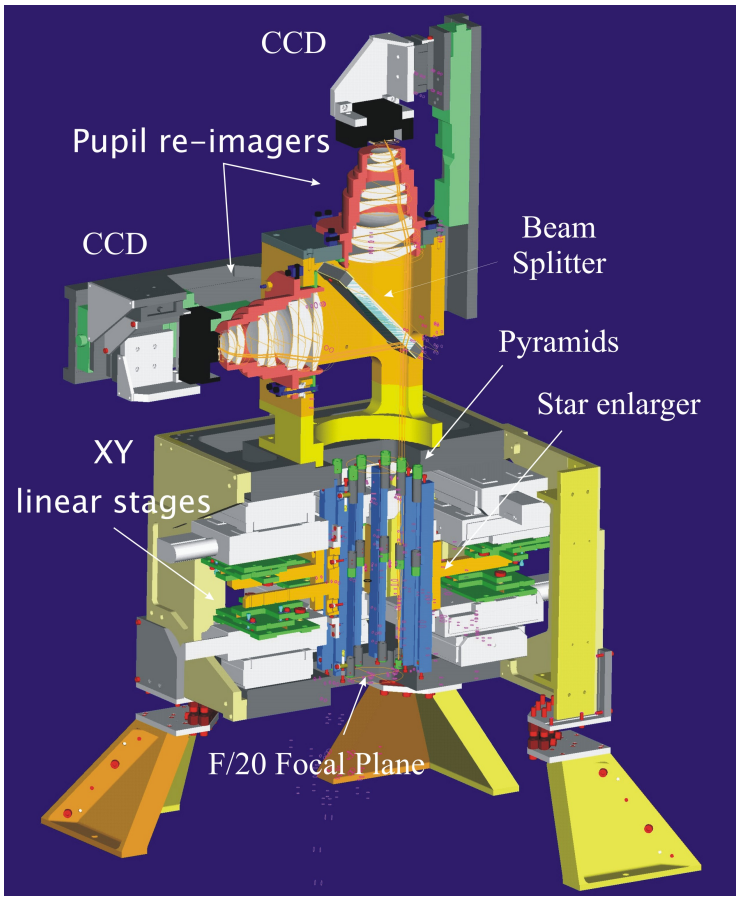

Figure 2.7: A section of a 3D image of the MHWS. Originally it was designed to accommodate two detectors conjugated to different altitudes in order to drive two deformable mirrors.

thus reducing the angular size of the pupil leaving the separation between the various stars across the FoV unchanged. This simple "trick" solves a known problem of the layer-oriented approach that is the size of the re-imaged pupils, which imposes the use of large detectors with massive binning.

Practical limits on the shrinking factor are imposed, for instance, by diffraction effects, which blur the re-imaged pupils. The basic principle is shown in Figure 2.8. The telecentric focal plane before the Mid-High wavefront Sensor is characterized by focal ratio F. The beam of each reference star is collimated by a lens of focal length f_1, producing a small pupil image. A second lens of focal length f_2, placed at a distance f_2 to the right of the intermediate pupil in order to preserve telecentricity, forms an enlarged image of the reference star with an equivalent focal ratio $F' = kF$¸ where the enlarging factor is given by $k = f_2/f_1$. At this position, a glass pyramid is

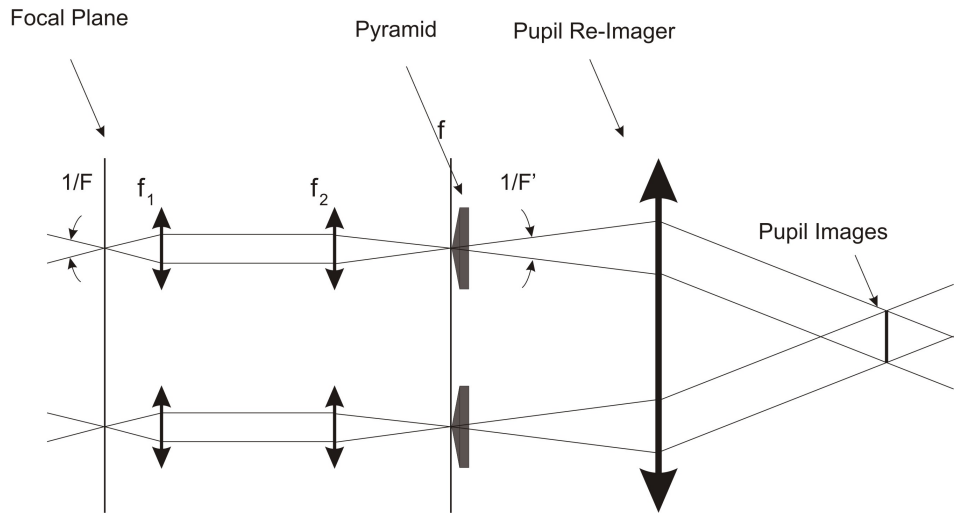

Figure 2.8: MHWS optical design concept. Only one pupil image is shown here; there are four pupil images.

placed in order to split the light into four beams, which are focused by a 7 lens objective of focal length f onto four pupil images. The re-imaged pupils corresponding to different reference stars are collected by the objective, which optically co-adds the light of the stars. The size of each re-imaged pupil is $s = f/F'$. The choice of the SE magnifying factor $k = 11.25$ and of the pupil re-imager focal length $f = 99$ mm derives from the pupil diameter, imposed by the requirement to fit the meta-pupil of the 2 arcmin FoV at the maximum conjugation altitude (15 km) onto a quadrant of the available detector (EEV CCD39, 80×80 pixel, pixel size 24 μm). With this choice each detector quadrant is filled by a meta-pupil, leaving a nominal 1 pixel thick edge around each meta-pupil and the meta-pupil at the highest conjugation range is mapped nominally onto 38×38 CCD pixels, corresponding to 19×19 sub-apertures in the 2×2 binning mode and approximately to 10×10 sub-apertures with a 4×4 binning. The angular divergence β of the beams at the output of the pyramids depends on the linear separation between the meta-pupils on the CCD and on the focal length of the objective. Its value is fixed to $\beta = 0.786°$, that corresponds to a pyramid vertex angle $\alpha = 1.535°$. Table 2.4 summarizes the main constrains, requirements and parameters of the MHWS designs.

2.2.1 The MHWS integration and alignment

The MHWF is divided into three main units and each unit is formed by components. Units and components need to be integrated and the optical

Input focal plane	F/20, telecentric, flat
Input FoV	2 arcmin
Working wavelength range	0.6 - 0.9 μm
Maximum number of reference stars	8
Minimum distance between two reference stars	$\approx$ 20 arcsec
Conjugation range	4km - 15km
Maximum (meta)pupil sampling	21×21
Star Enlarger FoV	$\approx$ 1.2 arcsec
k	11.25
f_1	14 mm
f_2	157.5 mm
f	99 mm
β	0.786°

Table 2.4: Basic requirements, constraints and main parameters of the MHWS design.

parts, to be aligned. The three main units are represented in Figure 2.9. They are: the reference stars selection unit, composed by the main structure with 4 legs and 16 linear stages for the Star Enlarger positioning in the field and the tip/tilt stages for the Star Enlarger mechanical alignment to the optical axis of the system; the 8 star enlargers, each formed by optics and optics holders; the pupil re-imager, formed by the 7 lenses objective with its support structure and the CCD camera with its position stages (X, Y and Z).

Assembly and mounting of components to units

Units and components were integrated and aligned in the laboratory of the Observatory of Bologna. A CCD camera with a smaller pixel size was used (Electrim 2000, 8 μm pixel size). The **eight XY pairs of the star enlargers positioning stages** were coupled and mounted on the main structure. The coupling process required some trials to obtain a group of eight stages with performance as good as possible in order to minimize the misalignment of the pupil images on the detector plane. Four pairs of stages were mounted on the lower plate of the main structure and the other four pairs on the upper plate. The maximum angle between the nominal direction of the SE axis and its actual direction (wobble) was between 11.7 arcsec and 18.9 arcsec. Each XY pair, after being orthogonalized with an error of about 8 arcmin PV, were mounted in such a way that:

- One of the axes (e.g. X) was parallel to a pre-defined direction (for instance defined by an edge of the square hole in the base plate of

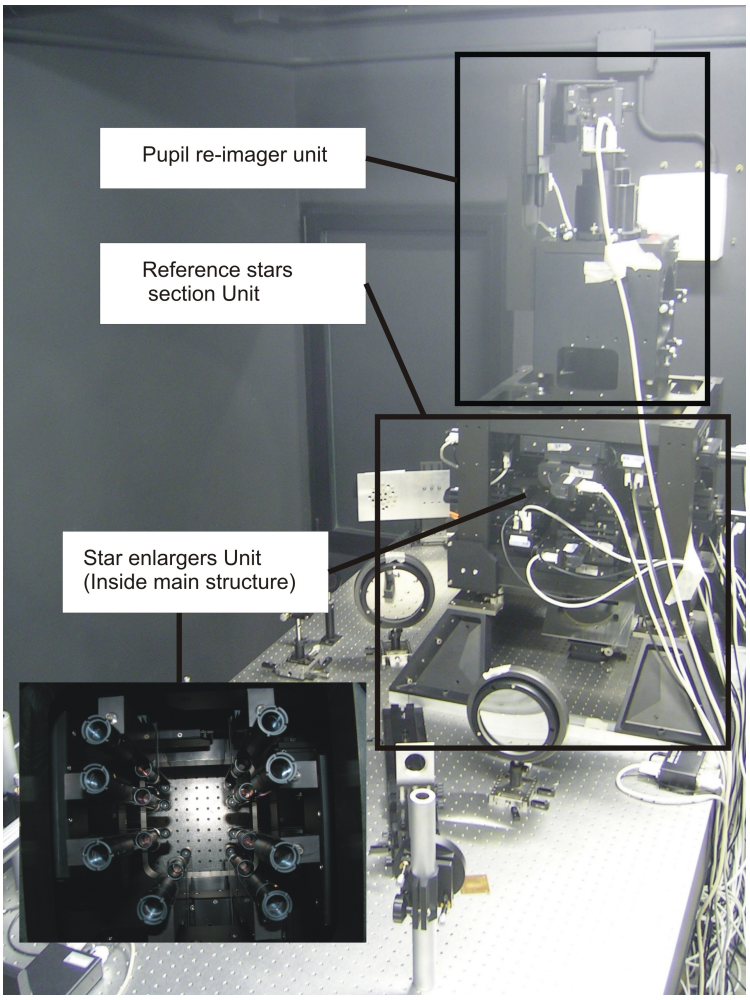

Figure 2.9: Picture of integrated MHWS with units indicated. The SEs are hidden inside the main structure of the reference stars selection unit. A top view of the eight mounted SE is depicted in the panel.

the main structure).

- The X and Y axes coverd their own quadrant (48.3 mm × 48.3 mm) and the two adjacent quadrants by ∼ 2 - 2.5 mm (the exact allowed value depends on the exact travel of each stage)

The assembly of each **SE** was done as explained in the following: each of the three elements that compose the SE, two lenses (diameter D = 6 mm and D = 12.7 mm) and one pyramid prism (diameter D = 12 mm), were placed inside its mount. The mount of the lens D = 6 mm and the mount of the pyramid D = 12 mm were connected to the SE support by retaining screws. Each of the optical components was optically aligned respect to the others and all of them respect to the mechanical axis of the star enlarger mount. The mount

of the lens D=12.7 mm was glued to the SE support. The SE tip/tilt stages were mounted onto the SE positioning stages (see Figure 2.10). Then the SE, already pre-aligned optically, were mounted onto the SE tip/tilt stages.

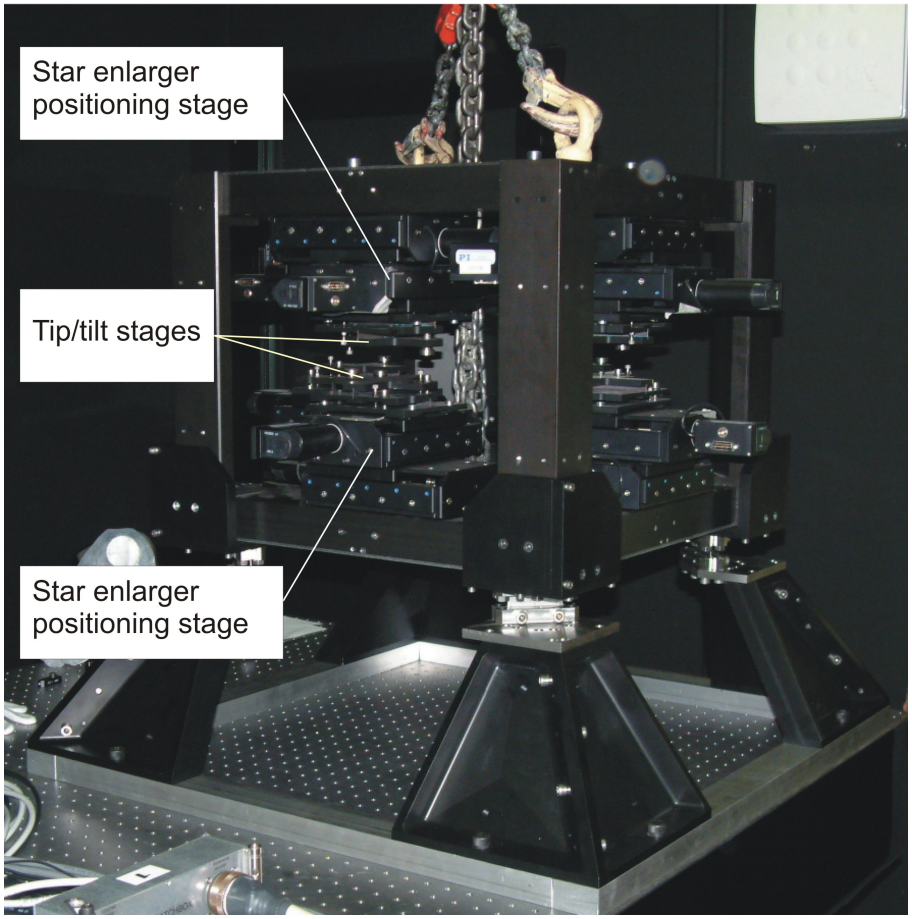

Figure 2.10: Two SE positioning stages (one attached to the lower plate of the main structure, one attached to the upper plate) and two SE tip/tilt stages.

The **objective** was then mounted on pupil re-imager support structure (see Figure 2.9). The centering and tip/tilt screws were set in order to perform a preliminary mechanical alignment of the objective, in preparation of the optical alignment (next section).

Definition of optical axis

The optical axis for the alignment of the MHWS optics (pupil re-imager objective and star enlargers) was materialized by a laser beam. This optical axis should ideally match the mechanical axis of the MHWS main structure, but thus tolerance is not very stringent since the SEs can be aligned in tip/tilt respect to the objective. The direction and centering of this mechanical axis

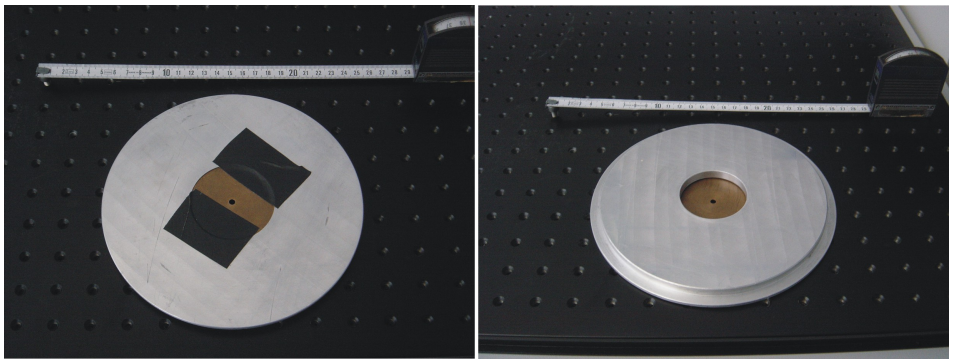

Figure 2.11: Left: down-looking side of alignment target. Right: up-looking size of alignment target; note the housing for the placement of a mirror (reflecting surface looking down).

may be identified by means of the target shown in Figure 2.11. This target was mounted below the MHWS main structure, at the level of the entrance focal plane; the target diameter matched the size of the square hole at entrance of the MHWS: the tightest the fit, the most precise was the identification of the centering of the mechanical axis. The target was held by means of clamps attached to the lower surface of the main structure. The hole at the center of the target defined the centering of the mechanical axis (Figure 2.11, left). On the upper part of the target (Figure 2.11, right) it was possible to accommodate a mirror, with its reflecting surface looking down: this mirror defined the planarity of the MHWS main structure and therefore the direction of the mechanical axis. The laser was adjusted in centering and tip/tilt until it passed through the hole in the target and it was orthogonal to the mirror. After this procedure, the laser beam identified the mechanical axis to be used as reference for the optical alignments.
The degrees of freedom to perform the laser beam adjustment described above may be the tip/tilt of the axial position of the 45° folding mirror below the MHWS and of another folding mirror in the optical setup on the bench.

Alignment of pupil re-imager objective

This procedure applies when the MHWS is aligned as a stand-alone unit and the optical axis has been defined as described in the previous section. The tilt alignment of the objective was performed by checking the spurious reflections of the incident laser beam, projected onto an observation screen. The decenter alignment was performed checking the beam transmitted by the objective and

projected onto the CCD camera at different focus positions: if the objective is centered to the beam, the position of the transmitted beam spot on the CCD camera remains fixed for every focus position. This procedure assumes that the parallelism of the focus movement to the laser beam axis has been verified before mounting the objective. In alternative, one may check the laser spot position on an observation screen before mounting the objective and comparing this reference to the position of the spot when the objective is mounted. When the MHWS has to be aligned to the LN warm optics, the objective may be assumed to be already aligned and may be used as a reference for the check of the optical axis tilt alignment.

Alignment of star enlargers integrated on Mid-High wavefront Sensor

The following steps describe the procedure for the alignment of the star enlargers when integrated on the Mid-High wavefront Sensor.

- **Alignment of rotation angle of pyramids**: a plate with a small central hole was placed in the aperture stop of the system or in an intermediate pupil image; the masked pupil was illuminated by a point source (fiber) and re-imaged onto the MHWS detector, through a given SE, forming four spots (one per pyramid face). The rotation angle of the pyramid was adjusted in order to align the four spots to the XY reference frame of the detector.

- **SE focus adjustment**: In order not to reduce the dynamic range of the MWHS and to avoid introducing large non common path aberration, the defocus measured by the sensor considering just static aberrations should be as small as possible. This was accomplished by adjusting the axial position of each star enlarger, nulling the defocus measurement on the image of a point source, placed for instance at the center of the entrance focal plane.

- **Alignment of SEs tip/tilt**: Since the tilt of a SE produces a shift of the four pupils on the detector, to ensure an acceptable superimposition of the pupil images produced by different SE, an accurate tip/tilt alignment has to be performed. A plate with a small central hole was placed in the aperture stop of the system or in an intermediate pupil image; the masked pupil was illuminated

by several point sources (fibers) across the field of view materializing the telescope field of view in the system. The masked pupil was re-imaged onto the MHWS detector, without SEs. The detector focus position was adjusted until the images of the hole (one image per point source) are superimposed. This procedure defines the MHWS conjugation to the pupil. The position of the focused image of the masked pupil was the reference for the following phase of alignment of the SEs. Each SE was positioned at the middle of the respective field quadrant, by positioning the XY positioning stage carrying the Star Enlarger itself at their mid travel position; this configuration was the optimal one from the point of view of the axis wobble due to the pitch and roll of the stages. Then the SE was aligned in tip/tilt using the tip/tilt stage (Figure 2.10), matching the center of gravity of the four pupil images on the detector to the reference position defined before, during the conjugation to the pupil plane. The relative alignment of the 8 SEs to this common reference was performed with an accuracy of 1/10 sub-aperture.

The three steps described might have to be iterated.

2.2.2 The MHWS verification tests

The MHWS was tested in the optical laboratory at INAF - Osservatorio Astronomico di Bologna by means of a lens-stop-lens telescope simulator to provide the F/20 focal plane at the entrance of the sensor (Figure 2.12). The guide star asterisms were provided by a set of 160 μm core optical fibers mounted on a dedicated plate.

The main requirements and specifications that have to be met after the alignment are summarized in Table 2.5.

Input focal Plane	F/20, telecentric, flat
WFE	$<$ 45 nm ($\sim$ 9.1 μm RMS pupil blur)
Star enlarger tilt	10 arcsec (1/5 sub-aperture)
CCD focus	0.001 mm

Table 2.5: Requirements for the MHWS.

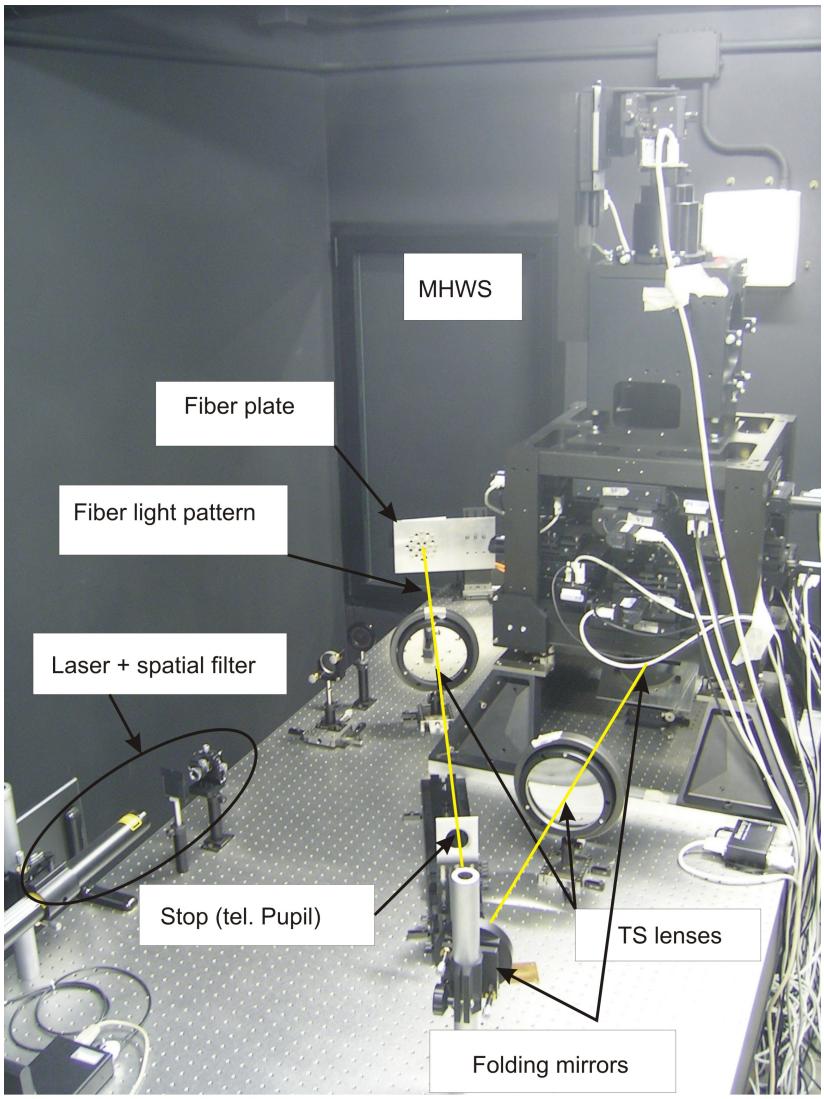

Figure 2.12: The MHWS test set-up.

Setup for the verification tests

In order to reproduce the telescope F/20 focal plane at the entrance of the MHWS, the telescope was simulated by means of a lens-stop-lens telecentric optical system (see Figure 2.12). A set of optical fibers was mounted on a plate with holes designed to emulate different asterisms of NGSs. A collimated laser beam represented the alignment reference. The F/num of the telescope simulator was measured using a pupil plane mask with two holes of known distance and measuring the distance between the two holes images on a CCD in two different out-of-focus positions. The measured F/num was 20.01. This number meets the requirement reported in Table 2.1. The position of the

entrance focal plane respect to a mechanical reference was also measured and the actual position matched the nominal one within 0.05 mm.

SE Alignment

The SEs defocus adjustment and tip/tilt alignment was done as described in Section 2.2.1. A SE mechanically positioned in the entrance focal plane was chosen as reference for focus adjustment of the other SEs. The residual defocus after regulation was 7 nm PV. The SEs were aligned at half range of the stages to provide the minimum tip/tilt caused by the motors' wobbling. A misalignment of the SEs translates into a bad superimposition of the pupil images on the CCD. Values of the measured RMS pupil blur are listed in Table 2.6.

Pupil	RMS blur
1	5 μm
2	5 μm
3	8 μm
4	6 μm
average	6 μm

Table 2.6: RMS of the four pupils center positions considering the 8 SEs.

The average RMS is around 6 μm, that corresponds to 1/4 of CCD39 pixels (24 μm). With a 2×2 binning it corresponds to 1/8 subaperture, in agreement with the requirements (listed in Table 2.5).

Pupil blur

Using a mask with holes in the aperture stop (see Figure 2.13), a measurement was taken with one star enlarger on axis. The central spot of the four re-imaged hole patterns was considered. The four spots presented a very small elongation towards the center (elongation $< 15\%$). The typical spot standard deviation (measured by a 2D gaussian fit) was in the order of $\sigma = 1$ pixel. The re-imaged hole dimension was 0.7 pixels. Removing in quadrature the intrinsic re-imaged hole size, gave a blur of about 0.7 pixels = 5.6 μm. This included the telescope simulator optical quality and chromatism and the blur due to the MHWS optics (SE diffraction, SE enlarging factor k, SE lens misalignment, vertex angle, chromatism, pupil re-imager optical quality). Considering also the pupil image blur measured by the geometric superimposition of the pupils of 8 SE (average blur $\sigma \sim 6$ μm), the two effects gave an overall pupil blur of $\sigma \sim 8.2$ μm, to

be compared with the expected blur of $\sigma \sim 9.1$ μm, correnspondig to 45 nm WFE, reported in Table 2.5. The measured value fully met the requirement, although it included the degradation due to the telescope simulator.

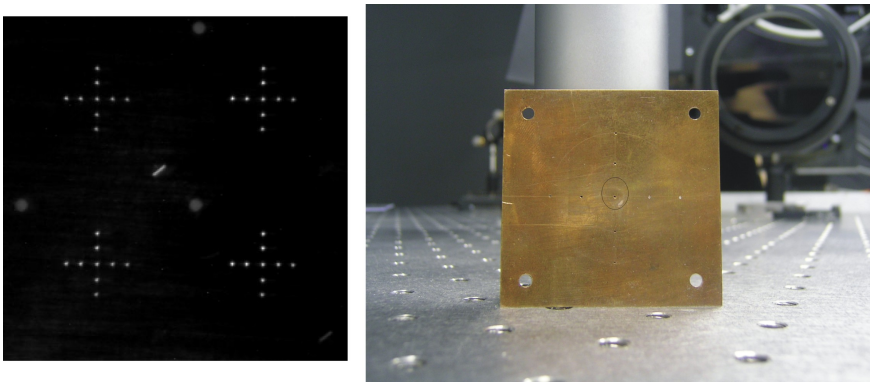

Figure 2.13: Image on the WFS detector of the pupil mask (right) and the pupil mask. Central hole is marked.

Pupil image quality and SE transmittance

The cosmetics through all SEs looked good. All the SE images showed the same feature present in Figure 2.14 in the upper right pupil. This feature was therefore due to the common path among all the SE (e.g. telescope simulator).

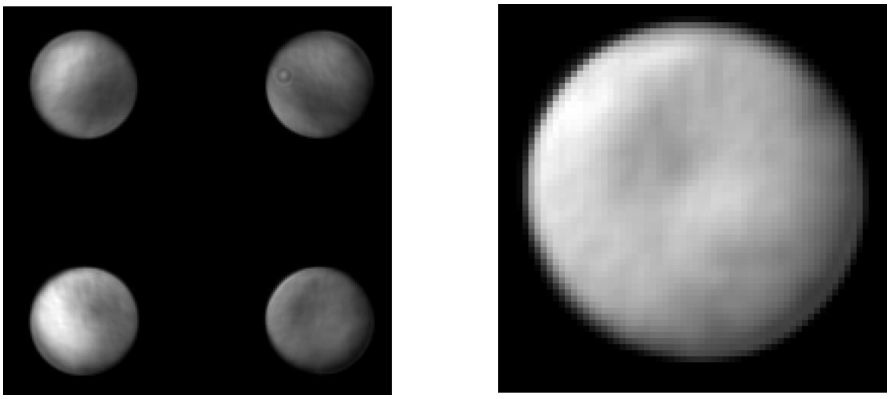

Figure 2.14: Four pupil images on the Electrim CCD (left panel); zoom of the bottom left pupil (right panel). Pixel size = 8 μm.

The absolute transmittance of the SE is reported in Table 2.7.

The measurements of the transmittance were compatible with $\sim 1\%$ light losses per surface, with a total of $\sim$20 surfaces (telescope simulator + MHWS). The repeated measurements of the transmittance of some SE, taken after several minutes, gave a repeatability estimate in the order of 5%.

Star Enlarger	Transmittance
1	82.6%
2	86.0%
3	84.4%
4	80.0%
5	83.7%
6	79.2%
7	80.3%
8	79.9%

Table 2.7: Absolute transmittance of the SEs.

Pupil dimension

In Figure 2.14 a pupil image is shown (right panel). The pixels looking black in the picture have a value of 0. Taking all the non-zero pixels and computing the diameter of a circle having the same area as the non-zero region, a diameter of 58.9 Electrim pixels was obtained, that converted into pixels of the CCD39 (24 μm), gave a pupil image diameter D = 19.6 pixels. The nominal pupil diameter on the CCD39 should be D = 18.3 pixels. The measured diameter has to be considered an upper limit, since various effects (e.g. SEs diffraction) tend to smooth the pupil edges and increase the pupil image diameter when the above criterion (all non-zero pixels considered) is adopted to measure the pupil diameter. In conclusion the pupil diameter met the requirement.

2.3 Integration of the MHWS to the LINC-NIRVANA post-focal relay

The final configuration of LN as described in Section 1.2.1 will be integrated on the final bench at the MPIA laboratories in Heidelberg. A preliminary setup was designed to test the post-focal relay (Section 2.1) including one single arm warm optics and MHWS (Section 2.2) in closed loop in order to ensure the performance of each single element in an almost final configuration, to check the alignment strategy, the software and electronics functionality. The Thesis work was to test and align the components of the setup in preparation of the future single-arm experiment, setting the standard for an alignment strategy for the final bench. The software and the electronics were not ready to be fully tested.

The aim of this section is to describe the laboratory setup (see Figure 2.15) for the future first single arm closed loop tests.

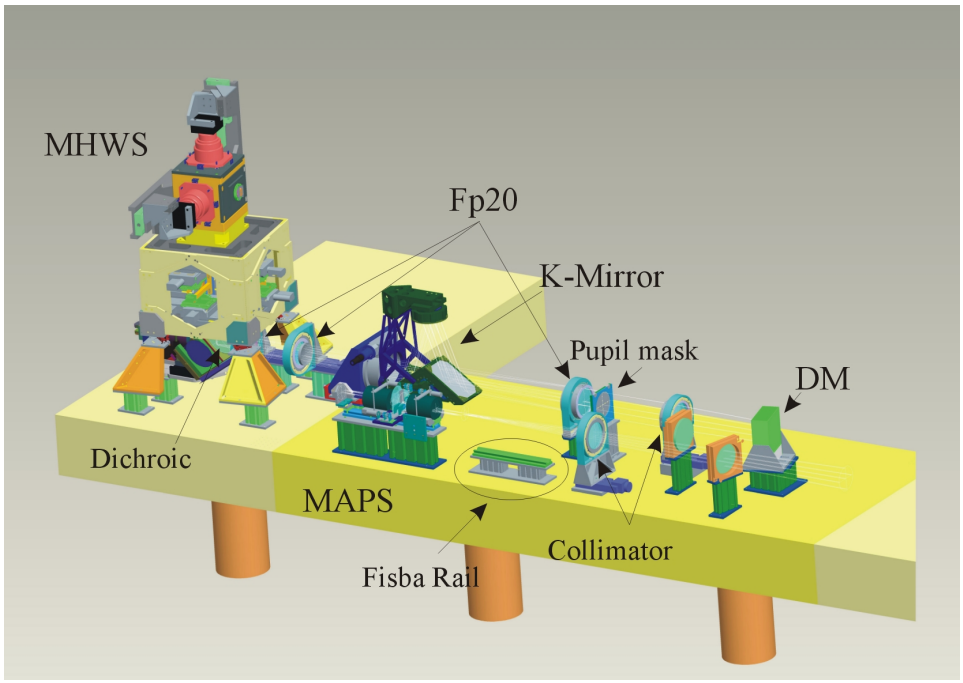

Figure 2.15: Setup configuration for the post-focal relay alignment and tests from a lateral view. Every component is shown as set in the MPIA laboratories.

The fiber plate (see Figure 2.16) was designed to reproduce the curvature of the focal plane of the LBT. 34 holes were designed to connect 12 fibers in several positions at the same time, simulating different asterisms of GS over the whole field of view. It is mounted on a completely motorized module: three translation stages for the positioning and one rotation stage to emulate the rotation of the field during the night.

The Multipurpose laboratory Atmospheric turbulence simulator MAPS (Hippler et al., 2006), together with the fiber plate, is an optical system that generates realistic atmosphere-like optical turbulence by means of rotating glass phase screens over a field of view of 2 arcmin. The fiber plate is one of three parts forming the MAPS unit. Two lens groups have the function of collimating the point sources and focus the F/15 beam. Between the two groups, the rotating phase screens can be adjusted to simulate the turbulence of a defined layer.

The F/15 beam is then collimated by the collimator optics and focused by the FP20camera that produces a telecentric flat focal plane at the entrance of the wavefront sensor. A mask holder is positioned in a pupil plane between the collimator and the FP/20 optics in order to repeat the procedures described

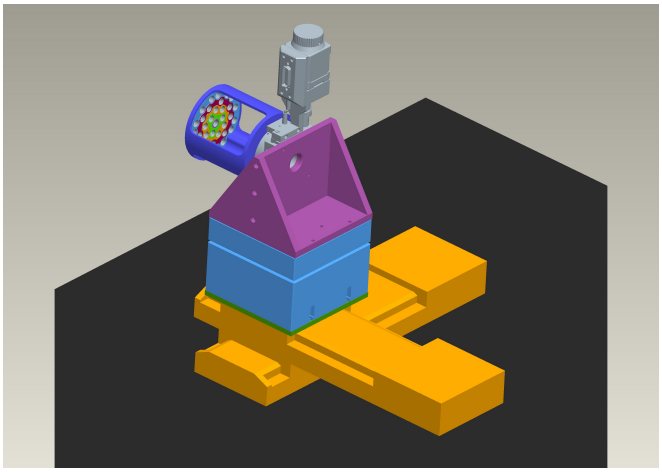

Figure 2.16: Fiber Plate for the simulation of the guide stars asterism. Different gray levels on the plate indicate different thicknesses of the plate in order to simulate LBT field curvature at the focal plane.

in Section 2.2.1 for the SE alignment and for the CCD conjugation to the pupil plane. Another similar mask, scaled to the metapupil dimension, can be applied to the DM surface for the CCD conjugation to a different altitude.

2.3.1 Alignment strategy

The alignment of the components of the post-focal relay was done defining a global optical axis with mechanical precision. The MHWS optical axis has to match the global one. This may be ensured by mechanical precision and, to some extent, by the degrees of freedom of the folding mirror under the MHWS. In general, it is not crucial that the centering of the global optical axis matches perfectly the MHWS optical axis: the only important requirements to fulfill are that:

- the beam of any reference star in the 2 arcmin FoV is intercepted by the pupil re-imager objective;
- the travel range of the SE positioning stages can reach any star in the FoV.

As a rule of thumb, a coarse mechanical alignment with an accuracy of the order of $\sim$1 mm is sufficient. The tilt between the global optical axis and the MHWS optical axis was adjusted using the tip/tilt adjustment of the folding mirror under the MHWS. The observable were the back-reflected spots produced by the spurious reflections of the laser beam onto the pupil re-imager

objective. The tolerance for this tilt alignment is of the order of ±1 mrad. The optical alignment of the warm optics respect to this global axis was done by means of transmitted and back reflected beam direction. A first positioning along the optical axis of the optics was done measuring the mutual distances between the components. The fine tuning was then obtained by means of a FISBA interferometer to check the collimation of the beam after the collimator and measuring the telecentricity of the f/20 beam at the MHWS entrance focal plane. This procedure was iterated. The optical quality was tested as described in Section 2.1.2 for the FP20 optics as a stand alone unit. The residual RMS measured due to the whole warm optics path, excluding the K-mirror, was around 40 nm (see Figure 2.17), as expected from the error budget.

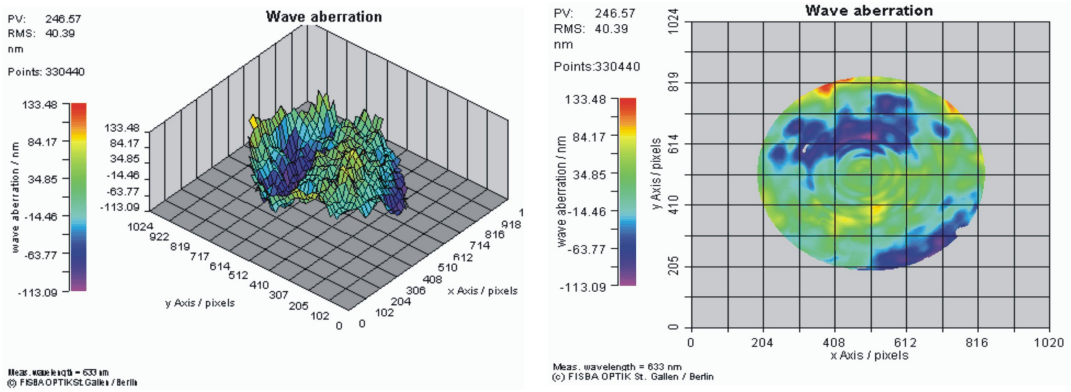

Figure 2.17: Optical quality of the system collimator + Deformable Mirror + FP20 optics + PatrolCamera beam splitter. Tip and tilt are subtracted.

2.4 Summary and future work

LN is an instrument that performs MCAO to correct the beams coming from the two telescopes of the LBT and combines them in a Fizeau interferometric mode. The part of the instrument dedicated to the WF correction is double (see Figure 2.1) and symmetric. The components of the LN warm optics (Section 2.1) and the MHWS for the mid-high layer turbulence correction were described in this Chapter. Each component was tested as a stand alone unit and then aligned to the rest of the setup. In particular one of the two MHWS was integrated and tested in the laboratory of the Osservatorio Astronomico di Bologna and, afterwards, delivered to the MPIA laboratory in Heidelberg. MHWS single components integration, alignment and verification was the subject of Section 2.2.1 while a detailed description of the verification tests

procedures and results is reported in Section 2.2.2. Section 2.3 described the procedure to align the MHWS to the post focal relay with the precision required in the LN FDR. In conclusion, the setup for the first single-arm experiment was aligned for the first closed loop tests, to be performed when the software and the electronics will be ready too.

The second MHWS will be integrated in Bologna, following the same described steps, in the next few months. Both the MHWSs will be integrated and aligned, together with the warm optics, to the rest of the instrument and, finally, delivered to the LBT. The first light is scheduled in 2012.

Chapter 3

Laser Guide Star spot Elongation

3.1 Sodium Laser Guide Stars

Adaptive Optics systems may provide diffraction-limited imaging with ground-based telescopes, measuring the wavefront aberrations due to the atmosphere by means of a suitably bright reference star and compensating for these aberrations by means of a deformable mirror (see Chapter1). In classical adaptive optics systems, based on a single natural reference star, such a star has to be located close to the target object, i.e. within the isoplanatic patch, so that the probability to find it is quite low. This probability defines the fraction of the sky where an efficient correction can be achieved (sky coverage), and for near infrared wavelengths it is few percent (Beckers, 1993). In this context the potential power of Laser Guide Star (LGS) adaptive optics, proposed by Foy & Labeyrie (1985), is clear. Laser beacons consist of the backscattered light generated by ground based laser beams passing through atmospheric constituents.There are two modes of scattering: (1) Rayleigh scattering, which is produced by air molecules and is useful at altitudes up to about 15 km; and (2) sodium resonance fluorescence, which occurs at an altitude of about 90 km. In the process of resonance fluorescence, sodium atoms are pumped by the laser irradiation from the ground state into an excited state, from which their natural decay produces the desired backscattered radiation. Although low-altitude Rayleigh scattering can provide much more backscattered light, the higher altitude of the mesospheric Sodium layer reduces the cone effect (Foy & Labeyrie 1985), i.e. maximizes the atmospheric volume sampled by the artificial source.

The use of LGSs in principle solves the problem of the lack of bright reference sources, but other difficulties arise. Apart from the above mentioned cone effect, that might be compensated using multiple reference sources (Foy & Labeyrie, 1985), a laser beacon cannot be used to determine the overall tilt which specifies the absolute direction of the object to be compensated. This is a consequence of the round trip of the light. In fact the position of the beam projected from the ground is randomly perturbed by atmospheric turbulence. When projected and viewed though the same telescope, a laser beam will always appear to be on axis no matter where the telescope is pointing, because the outgoing and incoming beams are deflected by the turbulence in exactly the same way. This is just a simplistic way to illustrate the problem, but for the purpose of this introduction there is no need to go into deeper details. To stabilize an image, it is necessary to use a separate reference source that is not perturbed by the atmosphere. Natural sources are an obvious choice. Overall tilt is the lowest order wavefront distortion component in single-aperture adaptive optics. The whole telescope aperture is used to collect the light and the integration time, for atmospheric tip/tilt only excluding wind shake effects, is relatively long, so the photon flux required from the guide star is considerably less than that for high-order compensation. In addition, the isoplanatic angle for overall tilt is greater than that for high-order compensation. For this reason the sky coverage with laser beacons stabilized by natural guide stars remains much greater than that of adaptive optics using natural guide stars alone. Another problem due to the usage of artificial reference stars is analyzed in this chapter and it is related to the perspective elongation of the LGS image, due to the vertical extension of the artificial source. On a 30-40 m class telescope, like the TMT (Nelson et al., 2006) and the E-ELT (Gilmozzi & Spyromilio, 2008), the maximum elongation θ_{elo} varies between few arcsec and 10 arcsec, depending on the actual telescope diameter, on the Sodium layer properties and on the laser launcher position. The spot elongation strongly limits the performance of the most common wavefront sensors. The centroiding error in a Shack-Hartmann wavefront sensor, for instance, increases proportionally to the elongation (in a photon noise dominated regime). To compensate for this effect a straightforward solution is to increase the laser power, i.e to increase the number of detected photons per subaperture. As illustrated in Section 3.3 this solution, although appealing in principle, presents drawbacks related, for

instance, to the availability of very powerful lasers. For this reason, alternative solutions to the spot elongation problem have been investigated. An interesting idea for a possible optical solution to the perspective elongation problem is presented in Section 3.4.

3.2 Geometry of laser guide star elongation

Referring to a Shack-Hartmann wavefront sensor, subapertures located far from the laser launcher see an elongated LGS image, pointing towards the laser launcher. The graphical representation of the elongation dependence on the laser launcher position respect to the subaperture distance from is shown in Figure 3.1.

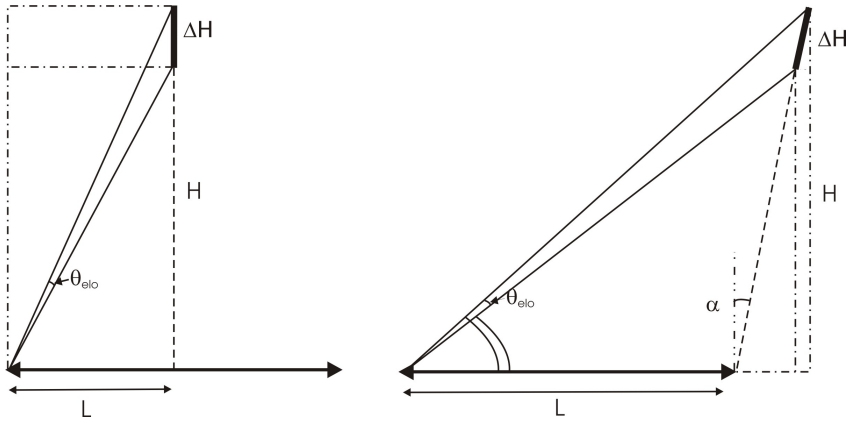

Figure 3.1: Elongation of the LGS image at a distance L (in this case at the edge of the telescope aperture) from the launch site for two different launching geometry: central and lateral. ΔH represents the thickness of the sodium layer, H is the mean altitude of the layer and θ_{elo} is the angular elongation.

In case of central launching scheme (Figure 3.1 left panel) the angular elongation is given by

$$\theta_{elo} \simeq \frac{L\Delta H}{H^2 + H\Delta H} \tag{3.1}$$

where ΔH is the thickness of the sodium layer, H is the mean altitude of the sodium layer and L is the distance between the pupil subaperture and the LGS launcher. The case of lateral launching scheme is a bit more complicate and Equation (3.1) becomes

$$\theta_{elo} \simeq \arctan\frac{H + \Delta H}{L + \alpha H} - \arctan\frac{H}{L + \alpha\,(H + \Delta H)} \tag{3.2}$$

where α is the launching angle of the laser (see Figure 3.1). In general, the elongation increases with the depth of the LGS (ΔH) and with the distance of the subaperture from the launch aperture of the LGS (L); the elongation decreases increasing the LGS height H. Each spot points in the direction of the laser launcher and its orientation depends only on the subaperture position respect to the laser launcher (see Figure 3.2). It is also evident that the elongation pattern results radial with respect to the pupil center only in case of central launching scheme.

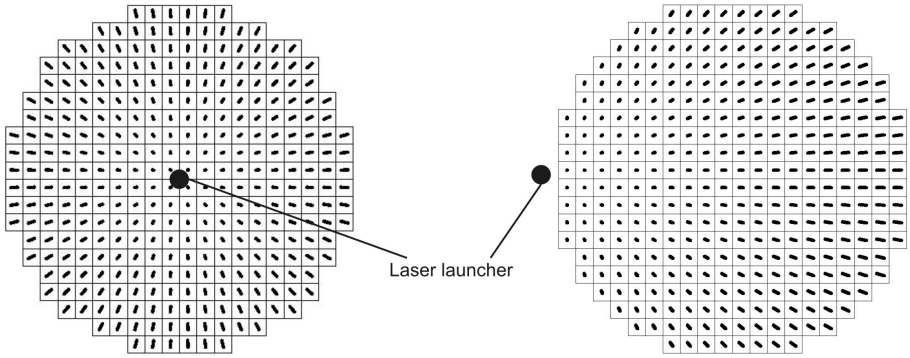

Figure 3.2: Elongation and orientation of the LGS images in each subaperture considering the two different launching geometry.

It is clear that this elongation, double in the case of lateral launching scheme, can dramatically affect the capability to measure the wavefront with a Shack-Hartmann wavefront sensor.

3.3 The Shack Hartmann Wavefront Sensor: Efficiency of centroid algorithms

Through numerical simulations was computed the measurement error on the OPD per subaperture considering three different centroid algorithms: Weighted Center of Gravity, Correlation and Quad-cell. The elongation pattern on a SH WFS in presence of spot elongation (i.e. for the 42 m E-ELT, Gilmozzi & Spyromilio, 2008) was computed in the case of LGS launched either from behind the secondary mirror (i.e. from the center of the pupil) or from the edge of the primary mirror. The measurement error on the OPD per subaperture was propagated to RMS wavefront error over the whole pupil,

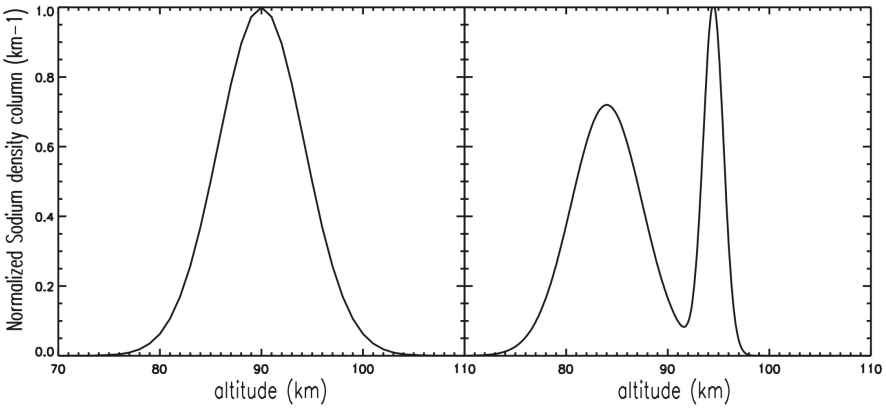

Figure 3.3: The two density profiles of the Sodium layer considered.

hereafter referred to as WFE, assuming a modal reconstruction on a Karhunen-Loeve (K-L) basis. The resulting WFE was then evaluated as a function of number of photons and RON.

3.3.1 Method

Sodium density profile

In order to understand what the image of a LGS looks like as seen from each subaperture of a Shack-Hartmann wavefront sensor, it is important to choose a model of the Sodium density profile. The density of the Sodium layer can change by a factor of two or more depending on the telescope site and the time of the year. Its mean altitude can change on a time scale of hours (O'Sullivan et al., 2000). Two different Sodium profile models (Figure 3.3), with shape similar to those presented in Drummond et al. (2004), were considered:

- Single Gaussian Sodium density profile, peak at $H = 90$ km and FWHM $\Delta H = 10$ km;
- Bi-modal Sodium density profile given by the sum of two Gaussians with the following characteristics: peak at $H = 84$ km and FWHM $\Delta H = 8.24$ km, peak at $H = 94.5$ km and FWHM $\Delta H = 2.35$ km.

Modeling elongated spots

The described Sodium profiles were used to simulate the spots seen by a SH WFS. Some examples of simulated spots are shown in Figure 3.4.

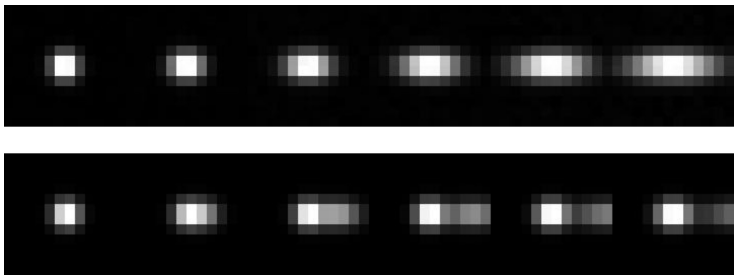

Figure 3.4: Simulated LGS images with different elongations, as seen from subapertures at different distances from the laser projector, considering a Gaussian profile (top panel) and a bi-modal density profile (bottom panel).

Two LGS launching schemes were considered: from behind the secondary mirror (central projection) and from the edge of the primary mirror (lateral projection). Central projection gives a perspective elongation pattern with radial symmetry respect to the pupil center, while lateral projection leads to a non-symmetric pattern with maximum elongation twice larger than in the former option (see Figure 3.2). The peak density of the Sodium layer was imaged at the center of the Field of View (FoV) of each subaperture.

The LGS spot imaged by each subaperture is modeled as follows:

- the starting point was a line source of length calculated accordingly to Equation 3.1 or 3.2 and with intensity distribution given by the adopted Sodium density profile;
- the line source was convolved by a seeing-like disk of angular size $\theta_s = 1.5$ arcsec, taking into account the round-trip propagation of the beam through the turbulent atmosphere (seeing $\sim$ 1 arcsec). This angular size corresponds to the width in the non-elongated axis.

The subaperture diffraction ($\theta_d \sim 0.24$ arcsec) was not considered in the spot model, as it is negligible with respect to the seeing effect, that always dominates over diffraction since the AO correction at the laser wavelength is quite poor.

A sequences of instantaneous spots is generated: each spot was characterized by a random jitter and was contaminated by photon noise and read-out noise (RON). The random offset was extracted from a Gaussian distribution, whose standard deviation may be tuned to simulate open or closed loop conditions. The photon noise was added to each pixel accordingly to a

Poisson distribution with a mean value equal to the pixel intensity; the RON was extracted from a Gaussian distribution of zero mean.

Different values of focal plane sampling and subaperture FoV may be adopted in the generation of the sequence, in order to evaluate their impact on the WFS performance. Depending on the chosen subaperture FoV, it may happen that the wings of the most elongated spots, especially for the the subapertures at the edge of the pupil, fall outside the FoV of the subapertures themselves. In a real system, this would translate into a light contamination of adjacent subapertures, a drawback that may be overcome using simple light baffling methods, for instance a diaphragm on the LGS image in an intermediate focal plane before the WFS. This baffling was always implicitly assumed here, so that the limited subaperture FoV was translated into a truncation of the spot wings, but not into a contamination of adjacent subapertures. The number of photons per subaperture referred to in the following includes also the photons blocked by the subaperture baffle.

Algorithm performance evaluation

The sequence of instantaneous spots, typically formed by 500 realizations, was analyzed by a spot position measurement algorithm. The algorithm result was compared to the known true position, thus obtaining a sequence of position differences, the RMS of which was the figure of merit for the algorithm performance evaluation. Each instantaneous spot was tested for detectability. For this purpose two checks were implemented (Thomas et al., 2006): the maximum intensity value of the spot was requested to be at least twice the RON and the calculated position had to be within $1-\sigma$ from the true position, where σ is the standard deviation of the best fit Gaussian to the long-exposure spot, obtained summing all the images in the sequence. When more than a certain fraction of images (in our simulations 50%, following Thomas et al., 2006) were rejected, the centroid measurements were considered to have failed and not reliable for those light conditions.

The main simulation parameters are listed in Table 3.1. The values of some parameters, like the number of pixels per subaperture and the pixel scale, are the result of an optimization presented in the next sections. The performance of the algorithms has been evaluated considering subapertures at difference distances from the laser launcher, in order to have a complete map

Telescope parameters	D = 42 m
Relative obstruction	0.3 linear
Non-elongated axis FWHM	$\sim$ 1.5 arcsec
Single Gaussian Profile	10 km FWHM @90 km
Double Gaussian Profile	8.24 km FWHM @84 km
	2.35 km FWHM @94.5 km
No. of subapertures across D	84
Subaperture FoV	12×12 pixel (central projection)
Pixel scale	0.75 arcsec/pixel
No. of photons per subap.	up to 2000
RON	1, 3, 5, 7, 9, 11 e^-/pixel
Number of K-L modes	5600

Table 3.1: Simulation parameters.

across the whole telescope pupil.

3.3.2 Weighted center of gravity

Algorithm description

The estimation of the position of the spot on the focal plane of each subaperture of the SH WFS is generally performed computing the Center of Gravity (CoG) of the spot. In this Section are analyzed the performance of a slightly different algorithm, the Weighted Center of Gravity (WCoG), proposed by Fusco et al. (2004). This algorithm is a maximum likelihood estimator of the spot position in presence of Gaussian noise. The expression of the x component of the spot position in a cartesian (x, y) reference frame is given by

$$C_x = \frac{\sum_{i,j} x_{i,j} W_{i,j} I_{i,j}}{\sum_{i,j} W_{i,j} I_{i,j}} \tag{3.3}$$

where $x_{i,j}$ is the x coordinate of pixel (i, j), $I_{i,j}$ is the intensity of pixel (i, j) and $W_{i,j}$ is a suitable weighting function. The y component of the spot position is similar. The theoretical weighting function (Fusco et al., 2004) is the instantaneous noiseless spot image itself. In the case of a small spot jitter in the subaperture, the weighting function can be assumed equal to the mean spot, i.e. to the average of the 500 realizations in the considered case.

The weighting function allows the attenuation of the noise effects, especially in the pixels with low signal, but it also introduces a distortion on the position estimation, proportional to the distance of the actual spot position from the center of the weighting function. In Thomas et al. (2006), a correction

factor, called γ factor, has been analytically calculated in the case of a Gaussian spot. Since it is interesting to analyze also the case of bi-modal and of more general spot shapes and since a good knowledge of the instantaneous spot and of the weighting function are crucial to calculate the γ factor (Thomas et al., 2008), instead of calculating a multiplicative γ factor, a calibration curve was empirically derived to compensate for the biasing effects due to the weighting function. For a given spot template, depending on the Sodium profile, the result of the WCoG applied to the template not contaminated with noise was plotted against the actual spot position for several known positions inside the subaperture FoV. The resulting plot was the calibration curve that allows the compensation of the bias. The spot template can be thought of as the average spot over a period of time over which the Sodium profile was approximately constant. The calibration curve depends on the spot elongation and therefore changes with the subaperture position in the pupil. In this way a curve like the one shown in Figure 3.5 is found for each subaperture. The calibration curve was fitted by a second order polynomial, which was used to retrieve the correct spot position for any position inside the FoV. This method easily allows the compensation of non-linear effects, due for instance to the truncation of the spot at the subaperture FoV edge or to sampling effects like in a Quad-cell scheme, as discussed later.

The results of the numerical simulations were verified using the analytical formulas of Thomas et al. (2008); the parameter N_{samp} of that paper, defined as the number of pixels per FWHM of the subaperture diffraction limited PSF, was assigned here the value $N_{samp} \sim 0.3$ (Figure 3.6).

A good agreement was found between the simulations and the analytical formulas. A slight disagreement was found in the case of low number of photons, probably because of the increased measurement noise due to the presence of negative pixels in the numerical simulations.

Algorithm optimization and performance

The measurement error on the OPD per subaperture was taken as a figure of merit for the optimization of the algorithm parameters and for the performance evaluation. The basic parameters were the focal plane sampling and the FoV of the subaperture. Given a subaperture FoV, the calculation may be restricted to a smaller window, to optimize the performance on particular Sodium profiles,

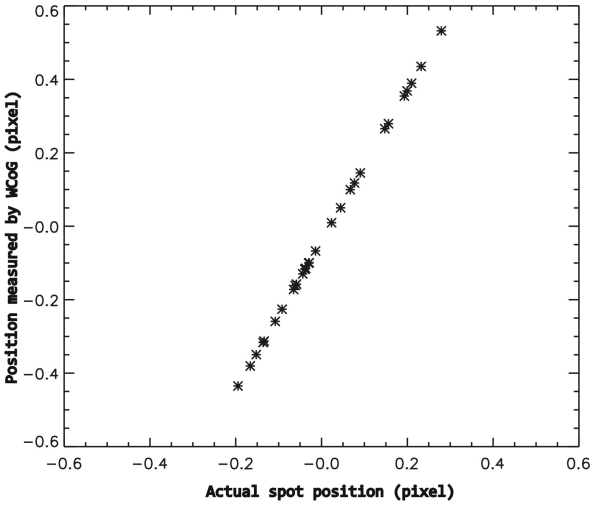

Figure 3.5: Example of calibration curve for the WCoG algorithm. A template is moved in a set of known positions and then the spot position is measured by mean of the WCoG. The estimated positions are plotted against the actual ones. The resulting plot is fitted by a polynomial function, that is used to correct the WCoG measurement for any position inside the subaperture FoV.

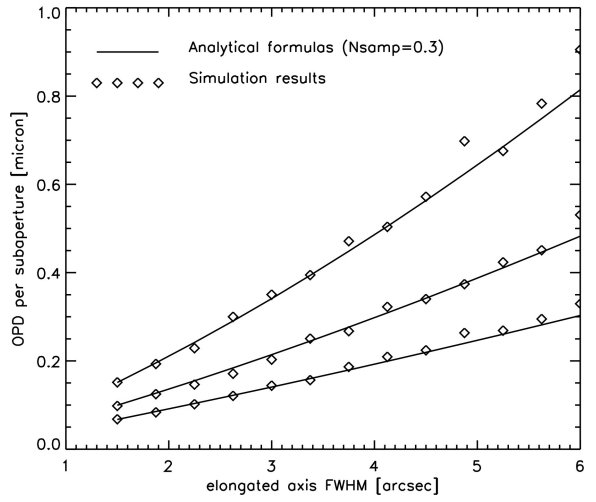

Figure 3.6: Comparison between OPD measurement error calculated by numerical simulations (symbols) and by the analytical formula (continuous line). Results are plotted vs. elongated axis FWHM. Central laser projection, RON = 3 e^-/pixel.

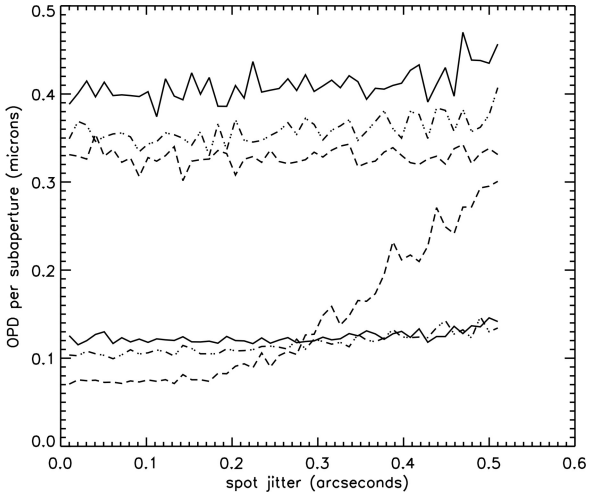

Figure 3.7: Weighted Center of Gravity algorithm sampling optimization: OPD measurement error in an edge subaperture for different values of spot jitter and for a Gaussian Sodium profile. Three different pixel scales are compared: 0.75 arcsec/pixel (solid lines), 1 arcsec/pixel (dot-dashed lines) and 1.5 arcsec/pixel (dashed lines). The three upper curves refer to the elongated axis, the three lower to the non elongated one.

like the bi-modal one, as it will be discussed later in this Section. For the optimization of the parameters, a reasonably high signal-to-noise ratio case was considered, corresponding to N_{ph} =500 and RON = 3 e^-/pixel. A central laser projection scheme was assumed.

The first step of the optimization was concerned with the sampling. Assuming a wide FoV, wide enough not to introduce any relevant truncation effect, the performance for three cases of sampling was evaluated: 0.75, 1 and 1.5 arcsec/pixel. Considering the non elongated spot width (FWHM = 1.5 arcsec, as indicated in Table 3.1), the first case corresponds approximately to the Nyquist sampling of the spot itself. The performance was evaluated in terms of error on the OPD measurement in an edge subaperture, as described in Section 3.3.1. It was considered a Gaussian Sodium profile for different simulation sets, corresponding to different values of the spot jitter, ranging from closed to open loop conditions. Accordingly to Tyson (1998), the maximum spot jitter of 0.5 arcsec that we have considered corresponds to a poor seeing condition of FWHM $\sim$ 2 arcsec, while a seeing of FWHM $\sim$ 1 arcsec roughly corresponds to a spot jitter of 0.3 arcsec. The results are shown in Figure 3.7, where the three upper curves refer to the elongated direction, while the three lower ones refer to the non elongated axis. From the elongated

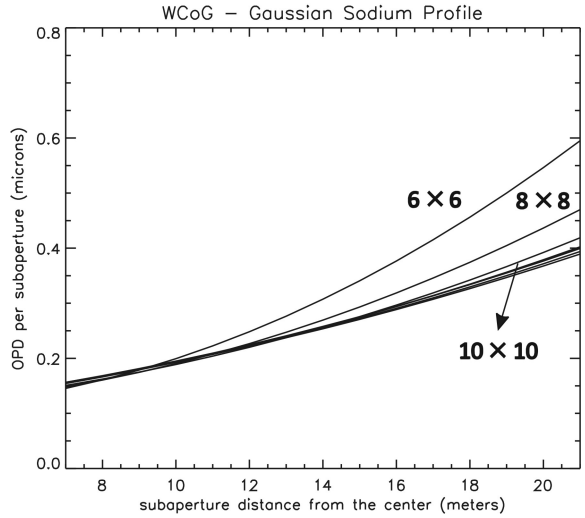

Figure 3.8: Weighted Center of Gravity subaperture FoV optimization: OPD measurement error as a function of the subaperture distance from the center of the pupil (central laser projection) for different cases of subaperture FoV. Pixel scale 0.75 arcsec/pixel. Gaussian Sodium profile.

axis, one might infer that the coarser sampling is the best, because it improves the signal-to-noise ratio per pixel. However it is clear that the non elongated direction may be affected by undersampling effects for the coarser pixel scale, which increases the measurement error for the larger spot jitter cases. For this reason, in the analysis the sampling of 0.75 arcsec/pixel was adopted in the following, as it assures a constant error even in the worst seeing conditions. However, just to mention it, also a coarser sampling of 1 arcsec/pixel looks very attractive, to slightly relax the photon flux requirements, without relevant drawbacks.

The second step of the optimization was concerned with the subaperture FoV. The analysis was performed on the two reference Sodium profiles (single Gaussian and bi-modal), assuming the sampling previously derived. The OPD measurement error was evaluated as a function of the subaperture distance from the laser projector, considering different subaperture FoV values, ranging from 6×6 to 20×20 pixels. The results for the Gaussian Sodium profile and central laser projection are shown in Figure 3.8. The optimal FoV for this profile is of the order of 12×12 pixels, since wider FoVs do not reduce further the measurement error. For lateral laser projection, the optimal FoV is of the order of 24×24 pixels. The results for the bi-modal Sodium profile are shown in Figure 3.9. In this case a smaller FoV is clearly advantageous: this

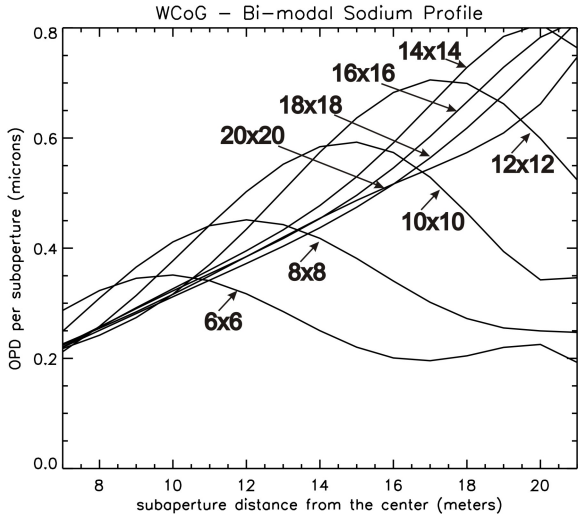

Figure 3.9: Same as 3.8, but for a bi-modal Sodium profile. The FoV is centered on the sharper component of the spot.

may be explained considering that a FoV as small as 6×6 pixels, centered on the sharper component of the bi-modal spot, translates into a mitigation of the spot elongation, although at the price of a loss of photon flux. This analysis shows that, for central laser projection, the optimal subaperture FoV, accounting for the different Sodium profiles considered here, is of the order of 12×12 pixels, but the calculation for the bi-modal case is more effective if restricted to a smaller window, extracted from the subaperture FoV.

The WCoG algorithm performance was then evaluated for different values of photon flux and RON with the parameters optimized before (0.75 arcsec/pixel sampling, 12×12 pixels FoV with windowing down to 6×6 for bi-modal profile). The results are shown in Figures 3.10 and 3.11.

3.3.3 Correlation

Algorithm description

The performance of an alternative centroid algorithm, the correlation, is analyzed in this paragraph . This algorithm computes the correlation function between the simulated instantaneous spots and a template. The most suitable template is a noiseless spot image fixed in a reference position (for instance the center of the FoV in the subaperture focal plane) that, in the case of a small spot jitter, can be assumed equal to the mean spot, i.e. to the average of the 500 realizations in this case. The correlation function has a peak in

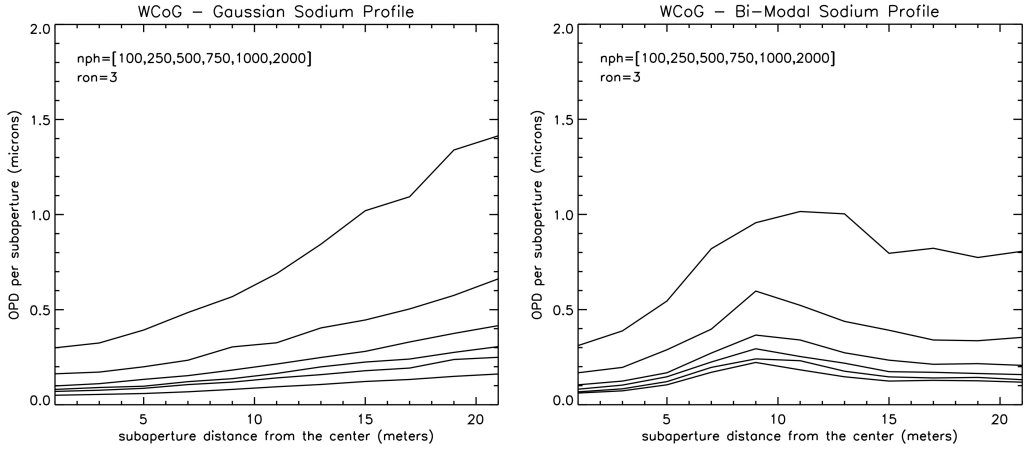

Figure 3.10: OPD measurement error as a function of the distance of the subaperture from the pupil center, for central laser projection. The OPD error is parametric in terms of the number of photons per subaperture, ranging from N_{ph} =100 to N_{ph} =2000. The lowest curve in each plot refers to the highest number of photons. RON = 3 e^-/pixel, sampling 0.75 arcsec/pixel. Left: Gaussian Sodium profile, subaperture FoV = 12×12 pixels. Right: bi-modal Sodium profile, window size 6×6 pixel.

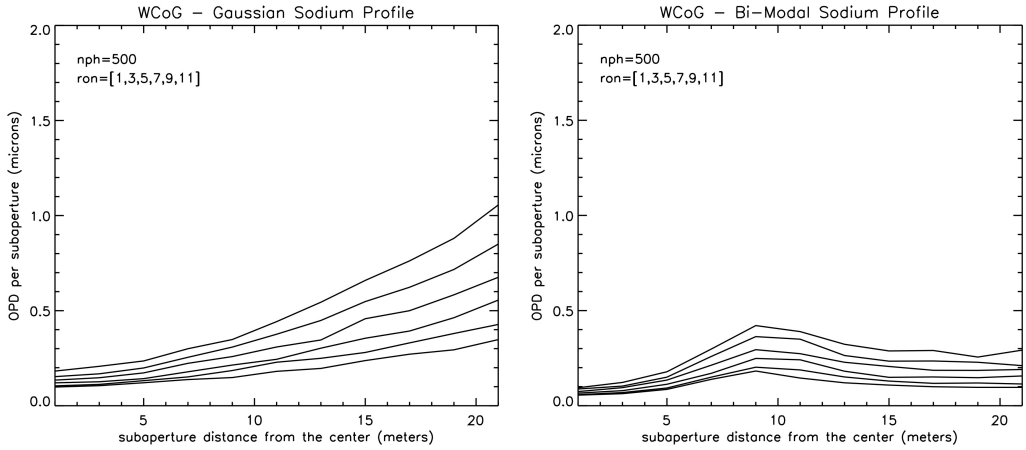

Figure 3.11: Same as Figure 3.10, but curves are parametric in terms of RON, ranging from RON = 1 e^-/pixel to RON = 11 e^-/pixel. The lowest curve in each plot refers to the smallest value of RON.

a position corresponding to the offset between the instantaneous spot and the template. In order to find the maximum of the correlation function with sub-pixel precision, the correlation function can be interpolated, through sinc interpolation for instance, over a finer grid (n times finer than the grid over the spot image is defined, i.e., the pixels in the subaperture), where 1/n represents the required level of accuracy in pixel units. In case of Gaussian sodium profile, the truncation of the spot in subapertures far from the laser launcher position, where the image of the LGS reaches the maximum elongation, introduces a bias in the correlation function computation (due to the different width of the instantaneous moving spot and the template). To evaluate the effects of truncation on the performance of the algorithm, for a given spot template, the result of the correlation between the instantaneous spots and the template not contaminated with noise was plotted against the actual spot position for several known positions inside the subaperture FoV. The resulting plot gave a curve for compensation of the bias. This procedure was the same described for the Weighted Center of Gravity in Section 3.3.2. Even if the results look promising, the speed of the algorithm is seriously problematic.

Algorithm optimization and performance

As done for the the Weighted Center of Gravity, the FoV of the subaperture was optimized in order to improve the algorithm performance. The focal plane sampling considered was 0.75 arcsec/pixel (to sample the FWHM of the non elongated axis with at least 2 pixels). A reasonably high signal-to-noise ratio case was considered, corresponding to N_{ph} =500 and RON = 3 e^-/pixel. A central laser projection scheme was assumed.

The OPD measurement error was evaluated as a function of the subaperture distance from the laser projector as for the Weighted Center of Gravity considering different subaperture FoV values, ranging from 6×6 to 14×14 pixels. The results for the Gaussian Sodium profile and central laser projection are shown in Figure 3.12. In the case of the considered bi-modal sodium profile, the computation of the centroid in a smaller window extracted from the subaperture FoV does not significantly improve the performance (see Figure 3.13). A satisfactory FoV in the case of Gaussian sodium profile is of the order of 12×12 pixels, since wider FoVs do not reduce dramatically the measurement error while decrease the speed of centroid computation of

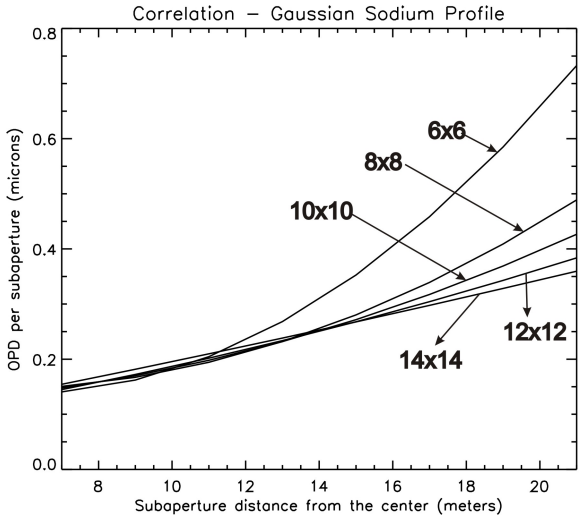

Figure 3.12: Correlation algorithm subaperture FoV optimization: OPD measurement error as a function of the subaperture distance from the center of the pupil (central laser projection) for different cases of subaperture FoV. Pixel scale 0.75 arcsec/pixel. Gaussian Sodium profile.

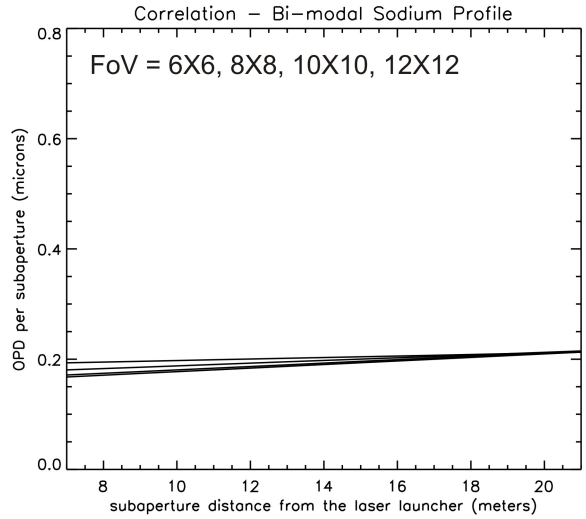

Figure 3.13: Correlation algorithm subaperture FoV optimization: OPD measurement error as a function of the subaperture distance from the center of the pupil (central laser projection) for different cases of subaperture FoV. Pixel scale 0.75 arcsec/pixel. Bi-modal Sodium profile.

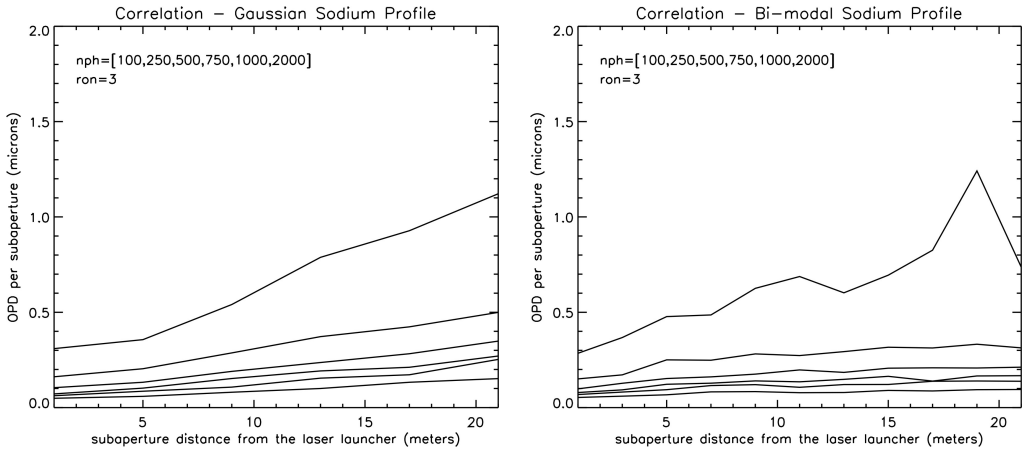

Figure 3.14: Quad-cell algorithm OPD measurement error as a function of the distance of the subaperture from the pupil center, for central laser projection. The OPD error is parametric in terms of the number of photons per subaperture, ranging from N_{ph} =100 to N_{ph} =2000. The lowest curve in each plot refers to the highest number of photons. RON = 3 e^-/pixel, sampling 0.75 arcsec/pixel. Left: Gaussian Sodium profile, subaperture FoV = 7.5". Right: bi-modal Sodium profile.

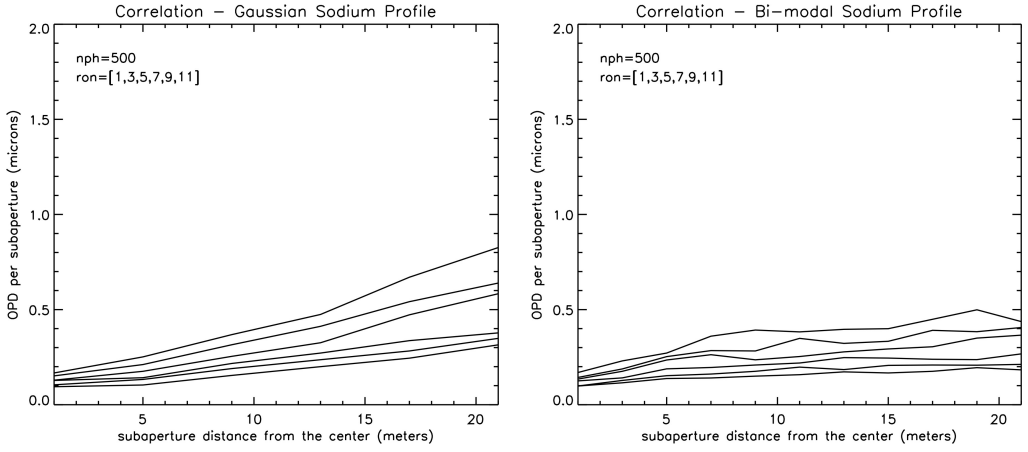

Figure 3.15: Same as Figure 3.10, but curves are parametric in terms of RON, ranging from RON = 1 e^-/pixel to RON = 11 e^-/pixel. The lowest curve in each plot refers to the smallest value of RON.

the algorithm. The FoV has to be doubled when a lateral launching scheme is considered. The Correlation algorithm performance are summarized in Figures 3.14 and 3.15, where the OPD error per subaperture are represented for different values of photon flux and RON with the parameters optimized before (0.75 arcsec/pixel sampling, 12×12 pixels FoV).

3.3.4 Quad-Cell

Algorithm description

The simplest arrangement to measure the spot displacement in a Shack-Hartmann WFS is to use a quadrant detector consisting of two orthogonal bi-cells (quad-cell), for each subaperture. The quad-cell configuration was simulated rebinning the LGS images on a 2×2 pixels grid. The displacement signals from a quadrant detector were obtained from the differential intensities between quadrants. If the outputs of the four quadrants are, for instance, a, b, c and d then

$$X_s = \frac{a - b - c + d}{a + b + c + d} \qquad\qquad Y_s = \frac{a + b - c - d}{a + b + c + d}$$

where s stands for *signal*. When using a quad-cell detector, the linear range of a Shack-Hartmann response is determined by the width of the spot. The linear range is limited to about a half of the FWHM of the LGS image. In this sense the elongation has the effect to improve the dynamic range in the direction parallel to the elongation (see Figure 3.16). In case of Sodium LGS reference sources, the instantaneous spots size depends not only on the seeing conditions but also on the sodium profile and on the perspective elongation and so it is unknown. Since the quad-cell response is very sensitive to the shape of the reference source, it needs to be calibrated during the observation monitoring the Sodium layer density variations by means of an additional and dedicated CCD with higher sampling. An image of the LGS, as seen from each subaperture and not contaminated by RON, can be therefore derived to trace the calibration curve plotting the measurements of the signals (x and y) against the actual position of the spot for several known positions inside the subaperture FoV. In the case described here, an image of the LGS sampled by 10×10 pixels with 0.75 arsec/pixel was used to trace the calibration curve. Since each quadrant requires only four pixels (2×2) for the spot motion

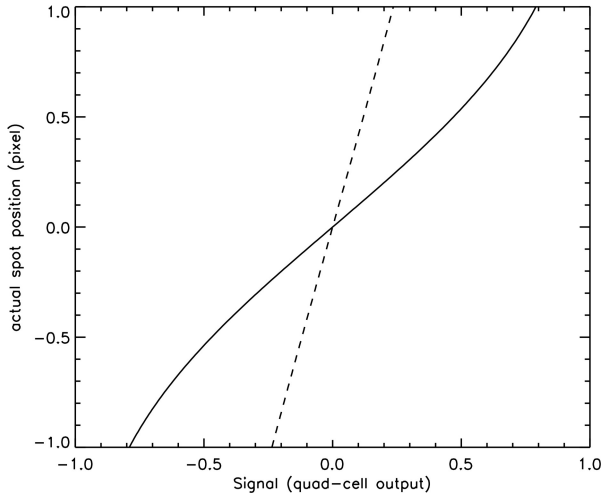

Figure 3.16: Example of gain curve for the quad-cell algorithm. A template is moved in a set of known positions and the signal is measured. The signals measurements are plotted against the actual positions of the spot. The Dashed line is the gain curve traced for the signal in the elongated direction (5" elongation represented here) and the solid line is the gain curve for the non elongated axis. The linear range is between approximately ± 0.5 pixels jitter from the subaperture center.

detection, the RON can be further reduced by a slow CCD readout and the dimensions of the CCD can be considerably reduced.

Algorithm optimization and performance

Unlike the two previous algorithm parameters optimization procedure, the quad-cell has a prefixed pixel sampling of the LGS image on the focal plane (2×2 pixels). We used the measurement error on the OPD per subaperture for the evaluation of the truncation effects on the OPD measurements and so for the subaperture FoV optimization. As for the other two algorithms, for the FoV optimization the following parameters were assumed: N_{ph} =500, RON = 3 e^-/pixel, central laser projection scheme and Gaussian sodium profile have been assumed.

The analysis was performed on the two reference Sodium profiles (single Gaussian and bi-modal) and the optimal subaperture FoV was established by the most stringent condition, i.e. by the Gaussian sodium profile model. The OPD measurement error hwas evaluated as a function of the subaperture distance from the laser projector, considering different subaperture FoV values, ranging from 3" to 15". The results for the Gaussian Sodium profile and central

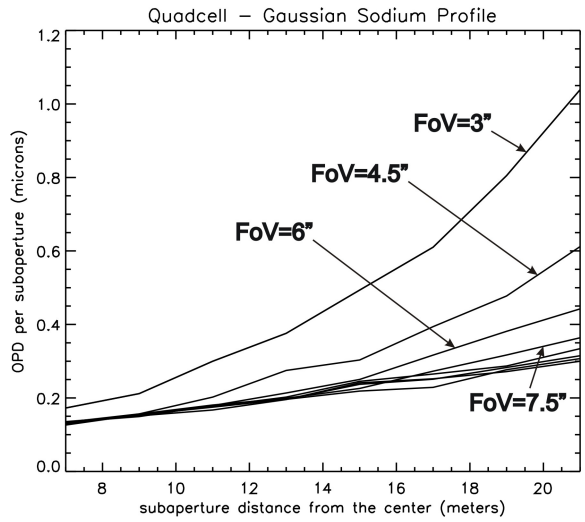

Figure 3.17: Quad-cell algorithm subaperture FoV optimization: OPD measurement error as a function of the subaperture distance from the center of the pupil (central laser projection) for different cases of subaperture FoV. Since the analyzed algorithm is Quad-cell, the image of the LGS in each subaperture in sampled by 2×2 pixels. Gaussian Sodium profile.

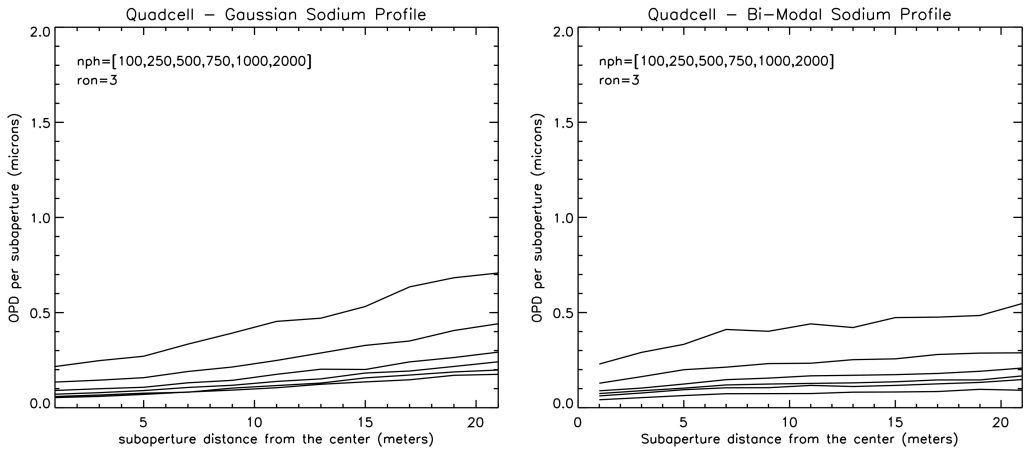

Figure 3.18: Quad-cell algorithm OPD measurement error as a function of the distance of the subaperture from the pupil center, for central laser projection. The OPD error is parametric in terms of the number of photons per subaperture, ranging from N_{ph} =100 to N_{ph} =2000. The lowest curve in each plot refers to the highest number of photons. RON = 3 e^-/pixel, sampling 0.75 arcsec/pixel. Left: Gaussian Sodium profile, subaperture FoV = 7.5". Right: bi-modal Sodium profile.

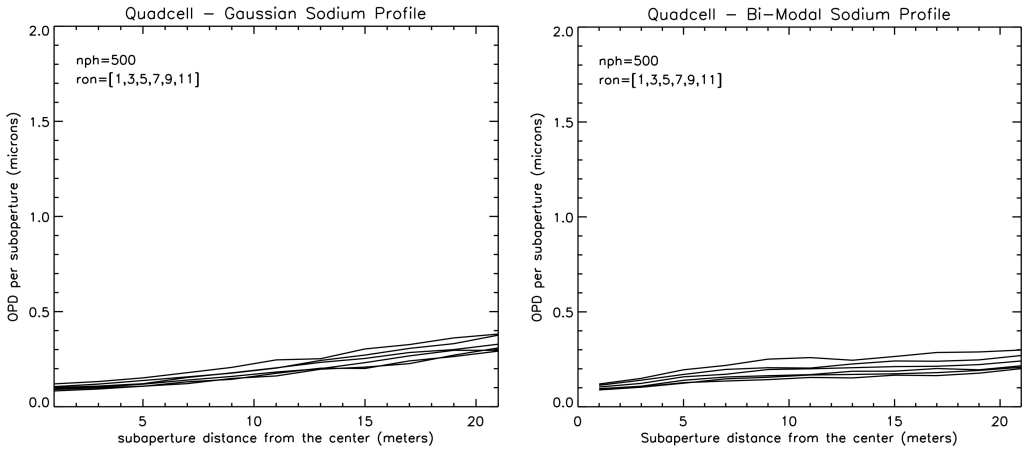

Figure 3.19: Same as Figure 3.10, but curves are parametric in terms of RON, ranging from RON = 1 e^-/pixel to RON = 11 e^-/pixel. The lowest curve in each plot refers to the smallest value of RON.

laser projection are shown in Figure 3.17. This analysis shows that, for central laser projection, the optimal subaperture FoV is of the order of 7.5". Larger FoV does not lead to evident improvements on the OPD error measurement.

As usual, quad-cell algorithm performance has been then evaluated for different values of photon flux and RON, once fixed the subapertures FoV. The results are shown in Figures 3.18 and 3.19.

3.3.5 Noise propagation

The wavefront on the whole pupil is reconstructed by mean of the OPD measurements per subaperture and hence the noise associated to the measurements is propagated to the reconstructed wavefront. The aim of this section is the translation of the OPD measurement errors calculated for different algorithms into RMS wavefront error (WFE). This propagation is performed assuming that the wavefront may be expanded as a linear combination of K-L polynomials; the considered number of modes, $N = 5600$, corresponds approximately to the total number of subapertures on the pupil of a telescope with the specifications listed in Table 3.1.

The OPD measurement problem and the wavefront reconstruction process can be expressed in a matrix-algebra framework (Rousset, 2004). The measurement equation is

$$\mathbf{s} = \mathbf{D}\mathbf{a} + \mathbf{n} \tag{3.4}$$

where $\mathbf{a}$ is a vector gathering the N unknown coefficients of the K-L modes, $\mathbf{s}$ contains a set of $2M$ OPD measurements (M is the number of subapertures) and $\mathbf{n}$ is a vector of measurement errors. The matrix $\mathbf{D}$ is a $2M \times N$ interaction matrix giving the wavefront sensor response to the K-L modes; apart from a normalization constant, its n-th column contains the average value of the derivative of the n-th K-L mode for each subaperture in one direction. The matrix $\mathbf{D}$ is assumed to be sorted alternating the x and y derivatives, although any other ordering is acceptable, provided the vector $\mathbf{s}$ is ordered accordingly.

A standard least-square reconstructor was considered, meaning that the reconstruction matrix is simply the generalized inverse of $\mathbf{D}$. Hence from Equation (3.4) we can write

$$\mathbf{a_{est}} = \mathbf{Bs} \tag{3.5}$$

where $\mathbf{B}$ is given by

$$\mathbf{B} = \left(\mathbf{D^T D}\right)^{-1} \mathbf{D^T}. \tag{3.6}$$

If the measurement noise $\mathbf{n}$ has a covariance matrix $\mathbf{C_s}$, the covariance matrix of the K-L coefficients is $\mathbf{BC_sB^T}$ and the wavefront error variance is the sum of the variances of the modal coefficients:

$$\sigma_a^2 = trace\left(\mathbf{BC_sB^T}\right). \tag{3.7}$$

The noise covariance matrix C_s is a block matrix of size $2M \times 2M$ and can be easily constructed with the following prescriptions. The measurement noise in different subapertures is statistically uncorrelated, so the covariance matrix is a block diagonal matrix. Furthermore, if the measurement of the spot position could be performed with respect to the principal axes $(\hat{x}, \hat{y})$ of the elongated spot (Figure 3.20), then the measurement noise in the two axes would be uncorrelated. However the spot position measurement is performed with respect to the axes of the (x, y) cartesian reference frame and the measurements errors in x and y are generally correlated: they may be retrieved from the measurement errors in the $(\hat{x}, \hat{y})$ reference frame applying a rotation matrix. The diagonal block referring to the j-th subaperture in the covariance matrix C_s has the following structure:

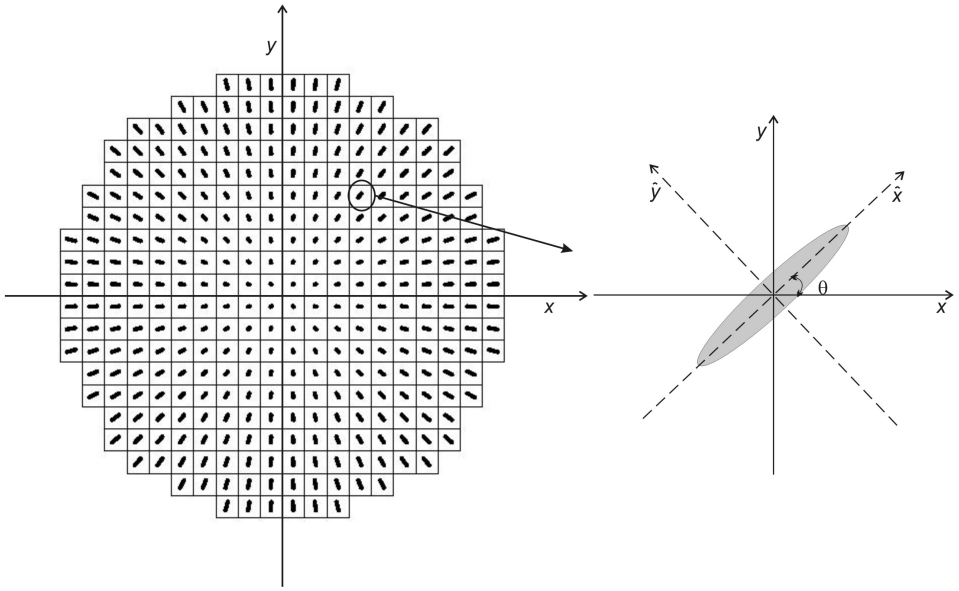

Figure 3.20: Elongation pattern for a LGS projected from behind the telescope secondary mirror. $(\hat{x}, \hat{y})$ is a reference frame defined by the spot elongation direction and obtained by rotating the frame (x, y) by an angle θ.

$$\begin{pmatrix} \sigma^2_{\hat{x}_j} \cdot a_j^2 + \sigma^2_{\hat{y}_j} \cdot b_j^2 & \sigma^2_{\hat{x}_j} \cdot a_j \cdot b_j - \sigma^2_{\hat{y}_j} \cdot a_j \cdot b_j \\ \sigma^2_{\hat{x}_j} \cdot a_j \cdot b_j - \sigma^2_{\hat{y}_j} \cdot a_j \cdot b_j & \sigma^2_{\hat{x}_j} \cdot b_j^2 + \sigma^2_{\hat{y}_j} \cdot a_j^2 \end{pmatrix} \tag{3.8}$$

where

$a_j = \cos\theta_j$

$b_j = \sin\theta_j$

and θ_j is the angle between the pre-defined global reference frame (x, y) and the local reference frame $(\hat{x}, \hat{y})$ defined in each subaperture by the direction of the elongation. An example of the elongation pattern on the whole aperture is shown in Figure 3.20.

The calculation of the WFE, i.e. the square root of the wavefront error variance defined by Equation 3.7, requires the evaluation of very large matrices with the adopted number of modes ($N = 5600$). For the design and optimization of the WFS, this evaluation has to be repeated for several cases of RON and of number of detected photons per subaperture. In order to speed up the process, we have applied a known property of the error propagation in a modal reconstruction approach (Hardy, 1998): the propagated WFE depends

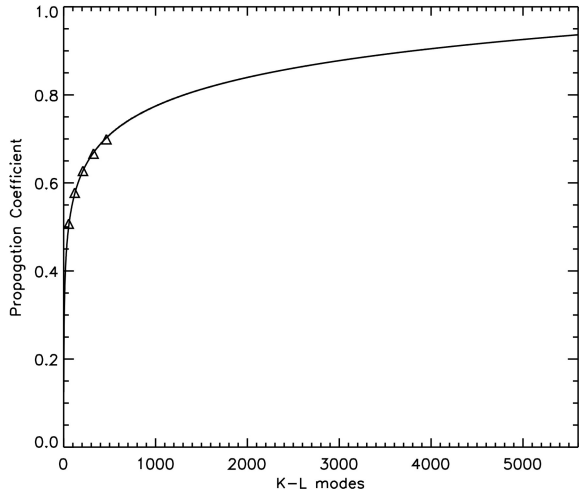

Figure 3.21: Error propagation coefficient in case of no central obstruction as a function of the number of modes for a case without spot elongation (diagonal measurement noise covariance matrix). Triangles represent some of the results of the calculations up to $N = 465$ modes; the extrapolated curve is the best fit logarithmic law described in the text.

on the number of modes N following a logarithmic law

$$\mathrm{WFE}\,(N) = a + b \log N \tag{3.9}$$

where a and b are constants. The calculation of the WFE has been thus performed following Equation 3.7 for relatively small number of modes, up to $N = 465$, and the results have been fitted by the logarithmic curve described by Equation 3.9; the best fit curve has been then extrapolated to the desired number of modes ($N = 5600$), representing essentially the maximum number of independent modes measurable with the telescope specified in Table 3.1. This method has been verified on a system with just 20 subapertures across the diameter: an excellent match has been found between the full computation of the WFE following Equation 3.7 and the approximated result obtained by the extrapolation of the best fit logarithmic curve.

The method proposed here was validated also in a limiting, though relevant, situation: the case without spot elongation, where the OPD measurement error is the same in all subapertures. Here the measurement noise covariance matrix is diagonal, $\mathbf{C_s} = \sigma_s^2 \mathbf{I}$, and the propagated error is

$$\sigma_a^2 = trace\left(\mathbf{B}\mathbf{B}^{\mathbf{T}}\right)\sigma_s^2 \tag{3.10}$$

where σ_s^2 denotes the measurement noise variance and the term $trace(\mathbf{BB^T})$ is the so-called error propagation coefficient, usually of the order of or lower than 1.

Figure 3.21 shows the behavior of the error propagation coefficient computed following Equation 3.7 for a sample of mode numbers (up to $N = 465$) and the best fit logarithmic curve (Equation 3.9), extrapolated up to $N = 5600$ modes. The error propagation coefficient estimated by this extrapolation is in very good agreement with the value found following the method proposed by Rigaut & Gendron (1992).

3.3.6 Required number of detected photons

Applying the method explained in the previous Section, the WFE in a number of cases with different detected photons per subaperture per frame and different values of RON using the described algorithms was calculated. Fitting the results for a given value of RON with a second order polynomial curve, the WFE was found as a continuous function of the number of detected photons. To evaluate the required number of detected photons per subaperture per frame, a target value for the WFE has to be defined. The study presented in this Thesis is based on the case of MAORY (Diolaiti et al., 2008), MCAO module for the E-ELT (Gilmozzi & Spyromilio, 2008). In the error budget of MAORY, the target for the WFE in closed loop is 100 nm. Considering the number of DMs, the number of LGSs, the noise reduction due to the closed loop correction, the target open loop WFE applicable to the present single channel analysis is 200 nm.

The analysis has been performed in three relevant cases:

- LGS projected from behind the telescope secondary mirror (maximum spot elongation $\theta_{elo} \sim 5$ arcsec)
- LGS projected from the edge of the primary mirror (maximum spot elongation $\theta_{elo} \sim 10$ arcsec)
- No elongation, a condition achievable in principle by range gating (Fugate et al., 1991) or dynamic refocus of a pulsed laser (Georges et al., 2008).

Figure 3.22 shows the results for the Gaussian profile of the Sodium layer and for the two laser projection configurations, central and lateral considering

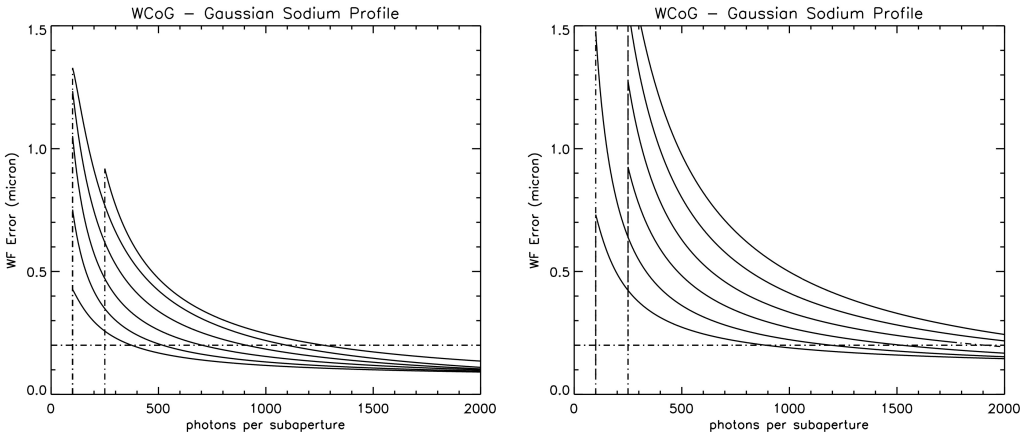

Figure 3.22: Weighted center of gravity centroid algorithm. Wavefront error vs number of detected photons per subaperture per frame for a Gaussian Sodium profile. The laser is projected from the center of the pupil (left panel) and from the edge (right panel). Different curves indicate different values of RON. The uppermost curve in each plot refers to the highest RON considered, i.e. RON = 11 e^-/pixel, and, in decreasing order, we find the curves relative to RON = 9, 7, 5, 3 and 1 e^-/pixel. The vertical lines represent the cut due to the detectability test described in Section 3.3.1.

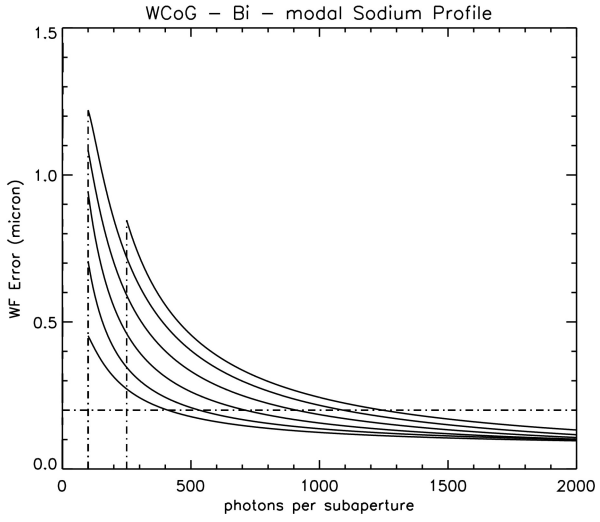

Figure 3.23: Same as Figure 3.22 for a bi-modal Sodium profile and considering only central laser projection. A 6×6 pixels window has been applied to the bi-modal spot, in order to select only the sharper component.

the weighted center of gravity algorithm. The noise is clearly larger for lateral than for central projection, by a factor ~ 2. This is true also considering other centroid computation algorithm. The target WFE in each plot is shown by the horizontal dashed-dotted line. Figure 3.23 shows the results for the bi-modal Sodium profile for the weighted center of gravity. In this case, the window used for the spot position calculations has been suitably optimized (see Section 3.3.2), in order to select the sharper component of the bi-modal spot. Comparing Figure 3.22 - left and 3.23, it may be noticed that the results are very similar, for a given laser projection configuration.

Figures 3.24 and 3.25 shows the results for the two Sodium profiles considered, Gaussian and bi-modal, when correlation (Figure 3.24) and quad-cell (Figure 3.25) algorithm are used for the spot position computation. Considering the particular bi-modal profile described above, composed by the sum of two Gaussian profiles, one narrow and sharp and the other wide, the results reported in the Figures are in agreement with the algorithms performance consideration in Section 3.3.2.

The results concerning the required number of detected photons to achieve the target value of WFE for different values of RON and in cases mentioned above are gathered in Table 3.2, 3.3 and 3.4 for the three considered centroid algorithms. A first evident conclusion is that the central laser projection is more effective than the lateral one from the point of view of the photon requirements. However the latter may be advantageous for other reasons, in particular for the background contamination due to the Rayleigh scattering of the upgoing laser beam in the lower atmosphere, that is stronger in the case of central projection. On the other hand, an additional aspect to investigate is the perspective elongation compared to the isoplanatic angle at the laser wavelength: the lateral launching is more sensitive to this problem than the central one. Finally it has to be noted that the considerable gain in the case without elongation is achievable by means of techniques as dynamic refocus, which is technologically challenging, or range gating, that wastes a non negligible fraction of the laser power.

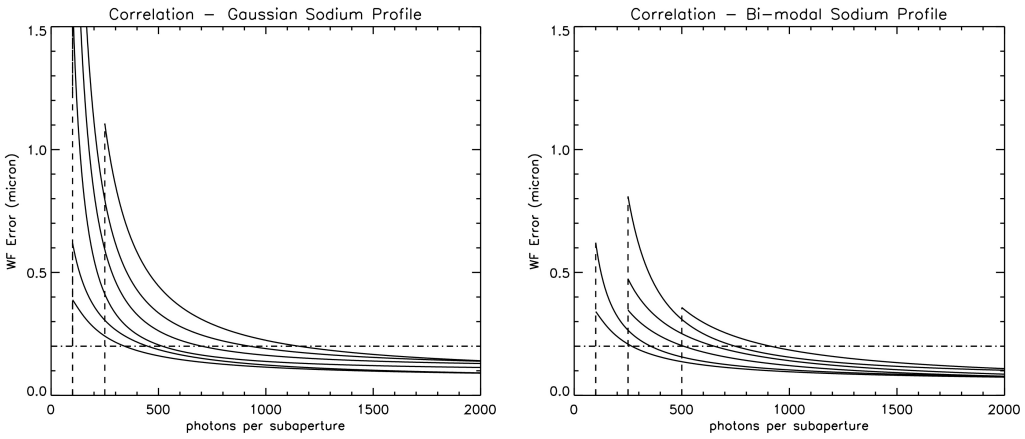

Figure 3.24: Correlation centroid algorithm. Wavefront error vs number of detected photons per subaperture per frame for Gaussian Sodium profile (left) and bimodal Sodium profile (right). The laser is projected from the center of the pupil. Different curves indicate different values of RON. The uppermost curve in each plot refers to the highest RON considered, i.e. RON = 11 e^-/pixel, and, in decreasing order, we find the curves relative to RON = 9, 7, 5, 3 and 1 e^-/pixel. The vertical lines represent the cut due to the detectability test described in Section 3.3.1.

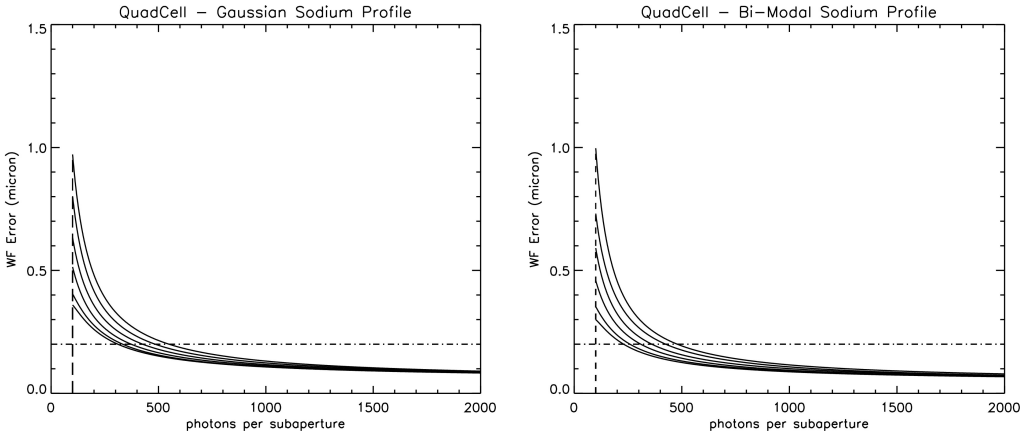

Figure 3.25: Quad-cell centroid algorithm. Wavefront error vs number of detected photons per subaperture per frame for Gaussian Sodium profile (left) and bimodal Sodium profile (right). The laser is projected from the center of the pupil. Different curves indicate different values of RON. The uppermost curve in each plot refers to the highest RON considered, i.e. RON = 11 e^-/pixel, and, in decreasing order, we find the curves relative to RON = 9, 7, 5, 3 and 1 e^-/pixel. The vertical lines represent the cut due to the detectability test described in Section 3.3.1.

RON	Central laser	Lateral laser	No elongation
1e$^-$	380	890	150
3e$^-$	520	1190	210
5e$^-$	700	1520	270
7e$^-$	910	1910	330
9e$^-$	1100	2200	410
11e$^-$	1200	2400	500

Table 3.2: Weighted center of gravity centroid algorithm. Number of detected photons per subaperture per frame required to achieve a WFE = 200nm per LGS. Three cases are considered: central laser projection, lateral projection and no spot elongation, a condition that might be achieved with a pulsed laser by range gating or dynamic refocusing. The results are presented for the Gaussian sodium profile. For the bi-modal sodium profile considered in this paper, assuming a proper windowing of the subaperture, the requested number of detected photons per subaperture is close to the results obtained in the Gaussian profile case.

RON	Gaussian profile	Bi-modal profile
1e$^-$	340	270
3e$^-$	450	350
5e$^-$	520	510
7e$^-$	700	650
9e$^-$	930	750
11e$^-$	1150	910

Table 3.3: Correlation centroid algorithm. Number of detected photons per subaperture per frame required to achieve a WFE = 200nm per LGS in case of central laser projection and gaussian sodium profile. The results are presented for the Gaussian sodium profile. For the bi-modal sodium profile considered in this paper, the requested number of detected photons per subaperture is lower than in case of Gaussian profile.

RON	Gaussian profile	Bi-modal profile
1e$^-$	310	230
3e$^-$	330	260
5e$^-$	375	310
7e$^-$	425	360
9e$^-$	480	420
11e$^-$	550	480

Table 3.4: Quad-cell centroid algorithm. Number of detected photons per subaperture per frame required to achieve a WFE = 200nm per LGS in case of central laser projection and gaussian sodium profile. The results are presented for the Gaussian sodium profile. For the bi-modal sodium profile considered in this paper, the requested number of detected photons per subaperture is lower than in case of Gaussian profile.

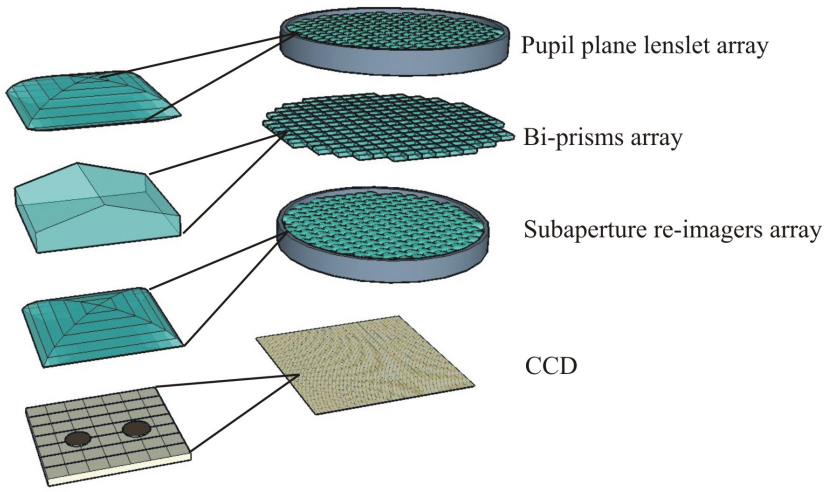

Figure 3.26: Bi-prisms array wavefront sensor concept.

3.4 The bi-prism Wavefront sensor

The spot elongation effect on classical WFS has been deeply discussed in previous Sections of this Chapter. The obtained results can be summarized in few words: increasing the laser power permits to compensate the loss of centroiding measurement accuracy due to the elongated shape of the spot in the Shack-Hartmann WFS focal plane. Lasers with the required power are still not available. In the context of a preliminary study for the MCAO module for E-ELT, alternative solutions were considered. This section presents a WFS concept that provides an optical solution to the perspective elongation problem (Schreiber et al., 2008 and Lombini et al., in preparation).

The optical design is based on an array of bi-prisms placed in the focal plane of a lenslet array; each bi-prism is aligned to the elongated spot produced by the corresponding lenslet; the spot is split into two beams, that are re-imaged into two micro-images of the subaperture itself; the difference in the integrated intensity of these two micro-images is proportional to the local WF slope.

Each subaperture sees the LGS from a different point of view. Consequently the images at the lenslet array focal plane have different elongations and directions, with the elongated axis pointing to the laser launcher position. For this reason the prisms forming the array in the focal plane have to be rotated one respect to the other in order to reproduce the same

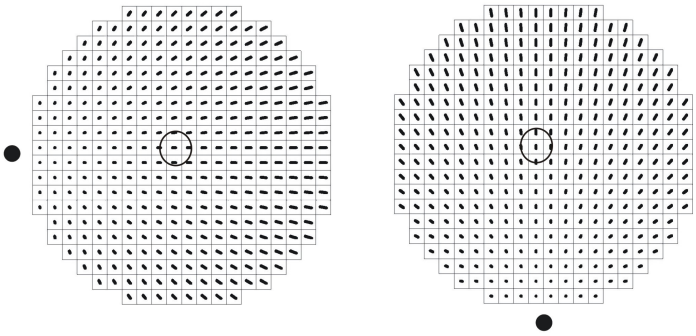

Figure 3.27: Examples of elongation patterns for LGSs launched from the edge of the primary mirror. The black circles indicate the laser launcher position. Small circles refer to elongation pattern of two different LGSs respect to the same subaperture. Two bi-prisms array measure local prime derivatives of the wavefront in two different direction that, in the represented case, are more or less orthogonal.

pattern as the elongated spots. The local slope in the direction orthogonal to the bi-prism edge is proportional to the difference of the integrated intensities of the two micro-images of the subaperture. In this way, however, the information about the local slope in the direction parallel to the elongation is lost. This information has to be retrieved somewhere else, for instance, from another bi-prism sensor looking at another LGS. In order to have linearly independent slope vectors in a given subaperture, it is necessary to project the LGSs from the edge of the aperture, otherwise the elongation pattern would look the same for all the LGSs (Figure 3.27).

Since the signal coming from more than one LGS has to be taken into account for the slope measurement in each subaperture, it was not possible to perform a single channel analysis, as for the SH case, to evaluate the measurement error. For this reason it was necessary to make some assumption on the tomographic reconstruction of a certain layer. The layer oriented approach offers a natural simplification of the problem. For a given subaperture at the level of the ground layer, where the footprints of the guide stars are perfectly superimposed, the local WF slope is given by the average of the slopes measured by means of all the reference stars. In an high layer, where the footprints of the reference stars are no more superimposed, an appropriate shift has to be applied before averaging the slopes.

A first order evaluation of the bi-prism WFS optical components was done

Telescope diameter	D = 42 m
No. of subapertures across D	84
Maximum spot FWHM	10 arcsec
Pixel per subaperture	4×4
Pixel size	24 μm
Lenslet 1	F/4, 96 μm pitch
Lenslet 2	F/1, 96 μm pitch
Bi-prism vertex angle	$\sim 60^\circ$

Table 3.5: Main requirements for the bi-prisms array optical elements.

for the E-ELT case. Since the lateral launching scheme has to be adopted, the maximum elongation reaches 10". The main parameters and requirements of the optical components are listed in Table 3.5.

3.4.1 Signal recombination and noise propagation

The aim of this Section is to illustrate a technique to combine the partial informations given by different bi-prisms sensors and retrieve the local WF slope measurement. It has to be underlined that, for simplicity reasons, a layer oriented approach was considered for the evaluation of the measurement noise propagation through the signal recombination process.

For simplicity, let us consider only two bi-prisms sensors that look at two LGSs launched as represented in Figure 3.27 (the black full circle represent the LGS position). For a given subaperture (for example the one marked with a circle in Figure 3.27), the two WFSs measure the local WF slope in two linearly independent directions. These two measurements of the 'partial local slope' can be represented as geometrical vectors with the same origin and forming an angle equal to the angle existing between the elongation directions of the two LGS images in the subaperture. These two vectors can be always orthogonalized. This means that the local slopes in two linearly independent directions can be always converted in local slopes in two orthogonal directions. When the number of measurements per subaperture is > 2, the local slope vectors have to be coupled two by two following the same procedure illustrated above. The pairs are rotated each by a proper angle in order to define a common reference frame (x, y); then the x and y slopes are averaged to obtain the local slope measurements for a given subaperture in a layer oriented mode.

The measurement error per subaperture per LGS as been calculated as

for a bi-cell:

$$\sigma_{bi-cell} = \frac{\pi^{3/2}}{2\sqrt{ln2}} \frac{\sqrt{N_{ph} + N_{px} \cdot N_{ron}^2}}{N_{ph}} \cdot \frac{\text{FWHM}}{\text{DIFFR}} \tag{3.11}$$

where N_{ph} is the number of detected photons,N_{px} the number of pixels in the subaperture, FWHM represents the dimension of the seeing limited spot on the bi-prism in the non elongated axis and DIFFR indicates the FWHM of the diffraction limited spot. The measurement error is propagated through the orthogonalization process. The slope measurement error in the common reference frame axis directions is given by

$$\sigma_x = \sigma_{bi-cell} \sqrt{\left(\cos\phi + \frac{\sin\phi\cos\theta}{\sin\theta}\right)^2 + \left(\frac{\sin\phi}{\sin\theta}\right)^2} \tag{3.12}$$

$$\sigma_y = \sigma_{bi-cell} \sqrt{\left(\sin\phi + \frac{\cos\phi\cos\theta}{\sin\theta}\right)^2 + \left(\frac{\cos\phi}{\sin\theta}\right)^2} \tag{3.13}$$

where ϕ is the angle between the two slope vectors of a given pair and θ represents the rotation angle to reach the common reference frame. Since the layer oriented approach was chosen as a simple tomographic reconstructor, the measurements relative to a given subaperture are averaged through the maximum likelihood method.

$$\sigma_{sub} = \sigma_{bi-cell} \sqrt{\left(\sum_{Npairs} \frac{1}{\sigma_x^2}\right)^{-1} + \left(\sum_{Npairs} \frac{1}{\sigma_y^2}\right)^{-1}} \tag{3.14}$$

3.4.2 Bi-prism sensor performance evaluation

In order to evaluate the performance of the bi-prisms array WFS, it is useful to compare its measurement error per subaperture with the Shack-Hartmann WFS. The OPD error per subaperture was computed using the same parameters for the two WFSs (number of subapertures across the telescope diameter, sodium profile, sampling, RON and total number of detected photons per subaperture). In first approximation the number of guide stars in the case of the bi-prisms sensor has to be doubled respect to the SH case. 8 LGSs launched from the aperture edge were considered for the bi-prisms WFS, while only 4 LGSs but with double power launched from the pupil center were used for the SH WFS. In the following table the parameters considered for the two approaches are listed.

	Bi-Prisms Sensor	**Shack-Hartmann**
RON	3	3
Pixel scale	0.75 arcsec/pixel	0.75 arcsec/pixel
No. of subapertures across D	84	84
Sodium density profile	Gaussian	Gaussian
Number of LGS	8	4
Maximum elongation FWHM	10 arcsec	5 arcsec
Launchers geometry	lateral	central
Subaperture FoV	4×4 pixel	12×12 pixel
No. of photons per subap. per LGS	50, 100, 200	100, 200, 400

Table 3.6: Parameters for the computation of the OPD error per subaperture for the two approaches.

The OPD error per subaperture was evaluated for two different layers, one at the ground level and the other at 12 km. In the case of the SH WFS, assuming a layer oriented approach, at the level of the ground layer, the OPD error per subaperture per LGS, computed with the weighted center of gravity algorithm (Section 3.3), was divided by the square root of the number of LGSs, that corresponds to averaging the OPD measurements. When an higher layer was considered, an opportune shift was applied. For the ground layer, the OPD error per subaperture was then propagated to RMS WFE over the whole pupil following the method illustrated in Section 3.3.5.

The Ground Layer

Using the parameters listed in Table 3.6 and the results of the simulations reported in Section 3.3 for the SH WFS, a map of the OPD error per subaperture for both the sensors was built (see Figure 3.28).

The radial behavior in the case of the SH WFS (right side maps) is due to the spot elongation trend across the pupil. The pi-prisms array (left side maps) shows only small fluctuations in the measurement errors due to the propagation through the local slope reconstruction process (see Section 3.4.1). Values of the WFE after the propagation over the whole pupil are summarized in Table 3.7.

Table 3.7 shows that the WFE in the case of the bi-prisms array WFS is roughly a factor of 1.5 better than for the SH WFS in the case of elongated spots and comparable to the SH WFS without considering elongation. It has to be underlined that in the case of a bi-prisms sensor the number of LGSs is

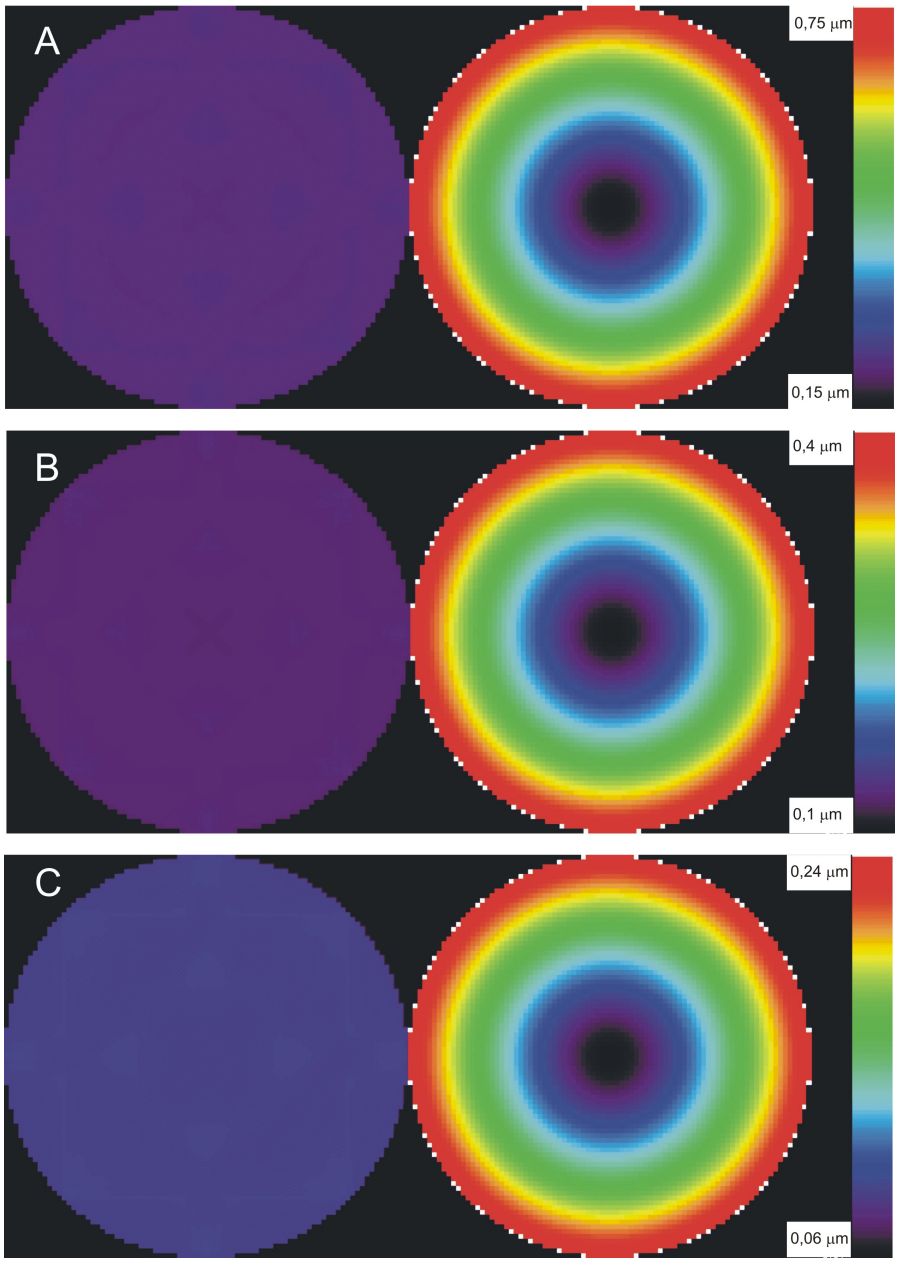

Figure 3.28: OPD error per subaperture in the ground layer using bi-prisms array (left) and SH WFS with WCoG (right). photons per LGS per subaperture are: 50 (panel A), 100 (panel B) and 200 (panel C) for the bi-prisms sensor and 100 (panel A), 200 (panel B) and 400 (panel C) for the SH.

Photons per subap. per LGS	Bi-Prisms sensor	S-H with elongation	S-H without elongation
50 - 100 - 100	0.18 μm	0.38 μm	0.16 μm
100 - 200 - 200	0.11 μm	0.21 μm	0.10 μm
200 - 400 - 400	0.07 μm	0.12 μm	0.06 μm

Table 3.7: Average wavefront error for ground layer using bi-prisms array sensor and SH wavefront sensor. The last column contains the average WFE in the case of a SH with the same number of subapertures, but without spot elongation (achievable with a pulsed laser coupled with range gating or dynamic refocus).

doubled, but the photons per subaperture per LGS is halved (respect to the SH case). It is also interesting to note that the SH WFS performance was evaluated here in the most favorable case of central projection: in the case of lateral projection the gain of the bi-prisms sensor with respect to the SH WFS is even larger than shown in Table 3.7.

The High Layer

When an higher layer is considered, an opportune shift has to be applied to the footprints before averaging the slopes per subaperture. The same procedure is valid for the measurement errors per subaperture. When a bi-prisms sensor is considered, at least two slope measurements per subaperture are required, but the regions at the edge of the metapupil in an high layer receive the signal from only one LGS. Moreover in some metapupil regions sampled by only two LGSs, the local slope vectors are almost linearly dependent so that the OPD error in that subaperture, through propagation, diverges. To discard these subapertures means to loose FoV. However in these subapertures the spot elongation is minimum. For this reason a possible solution is to replace the bi-prisms in these critical regions with pyramids (with four faces). The pyramids measure the WF local slope corresponding to that subaperture using the signal coming from only one LGS. The concept of this hybrid array sensor is shown in Figure 3.29.

This solution, even if appealing, does not fully solve the problem. In fact in the regions of the array filled with pyramids the elongation, even though small, translates into an unknown gain variable from one subaperture to the next. The bi-prisms do not suffer of this gain variability issue since they measure the slope only in the non elongated direction. In the framework of this section

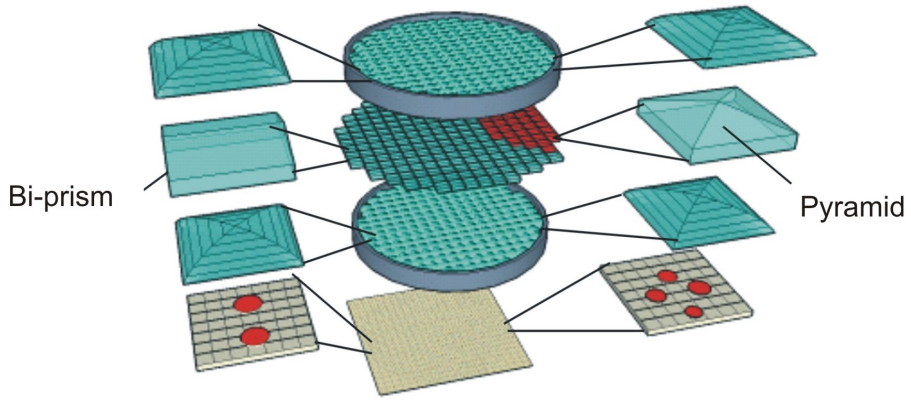

Figure 3.29: A possible solution to the loss of FoV due to the usage of a bi-prisms array in high layer reconstruction. In the region of the pupil where the elongation is less than a certain value, pyramids replace bi-prisms.

the effects due to this variable gain are neglected. Figure 3.30 shows the OPD error per subaperture maps for a reconstructed layer at 12 km.

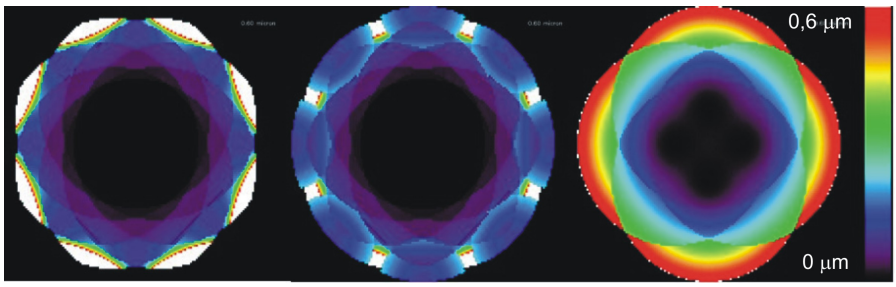

Figure 3.30: OPD per sub-aperture considering a layer at 12km. Left panel represents the case of a normal bi-prisms array considering 200 photons per subaperture per LGS; in central panel a hybrid array of bi-prisms and pyramids has been used; results for a normal SH WFS are reported in the right panel considering 400 photons per subaperture per LGS. The OPD error per subaperture has been cut at 0.6 μm (white pixels), corresponding to the maximum OPD error of the SH WFS.

Three cases are shown in Figure 3.30: the case of a bi-prisms array in its original version (without pyramids) on the left; the case of the hybrid array (bi-prisms + pyramids) in the center; the case of a SH WFS on the right. Again the number of detected photons per subaperture per LGS in the case of the bi-prisms array is halved respect to the SH case, while the number of LGSs is doubled. White regions in the maps indicate subapertures where the OPD error is greater than 0.6 μm, that is the maximum OPD error value in the SH case. This value was chosen to discard the subapertures in the bi-prisms array

sensor (hybrid and not) where the OPD error is too large.

The maps shown in Figure 3.30 give a clear idea on the capabilities of this WFS in terms of OPD error per subaperture also for an high layer. Improving the WFS design by means of an hybrid array also the sampled metapupil area in the case of the bi-prisms sensor and of the SH WFS are similar.

In conclusion the application of the bi-prisms WFS concept to a GLAO system for the E-ELT looks feasible and also promising. The bi-prisms WFS application to an MCAO system requires a better investigation concerning the high layers reconstruction. The feasibility of a bi-prisms array has not been investigated, although the optical parameters shown in Table 3.5 do not look particularly demanding. The bi-prisms sensor offers some notable advantages. First of all the detector size is much smaller: Table 3.5 reports that a 4×4 pixels region on the detector is enough to re-image the two subaperture images and measure the local slope. It is also true that the number of LGSs required by the bi-prisms array is roughly doubled respect to the classical SH case, but only half of the signal per LGS is requested.

Chapter 4

Application to the E-ELT case

The baseline choice for MAORY is the use of Laser Guide Stars (LGS), following the choice adopted in other MCAO systems (Gemini MCAO, NFIRAOS for TMT). The current concept of MAORY is characterized by two post-focal Deformable Mirrors (DM) conjugated to the high-altitude turbulent layers, that complement the high-order ground-layer correction and the field stabilization provided by the adaptive telescope. From the wavefront sensing point of view, the MCAO module is characterized by a multiple Sodium LGS wavefront sensor (WFS) for the high-order sensing, using 6 LGS, and a multiple Natural guide star (NGS) WFS, to measure the low-order modes, that determines the final sky coverage.

4.1 LGS wavefront sensor: first order design for MAORY

The effect of the LGS perspective elongation on the performance of a Shack-Hartmann WFS for a large aperture telescope has been analyzed in Chapter 3. Three different algorithms have been used for the spot position measurement in the subapertures: the Weighted Center of Gravity, the Correlation and the Quad-cell. The OPD measurement error in the subapertures has been propagated to WFE (RMS wavefront error) across the whole pupil, assuming a modal least square wavefront reconstruction; a fast method to perform this error propagation has been proposed and validated, improving the efficiency of the calculation for a system with a very large number of subapertures. The method proposed in Chapter 3 is based on a single channel approach, i.e. it allows the computation of the propagated wavefront error per single LGS, starting from the first order properties of the WFS (number of subapertures,

number of detected photons per subaperture, RON, focal plane sampling, subaperture FoV, calculation window).

The target WFE per LGS established by the MAORY error budget is 200 nm and 270 nm. These numbers come from the requirement of 170 nm WFE in closed loop, that translates in 200 to 270 nm open loop noise WFE depending on the hypothesis made on the loop temporal filtering. Different Sodium profiles have been considered: a Gaussian profile and a bi-modal one. It has been found that, with a suitable optimization of the WCoG algorithm performed by restricting the subaperture FoV in case of Bi-modal sodium profile, the performance is quite similar in the two cases. Correlation and Quad-cell do not need this optimization and for the particular bi-modal sodium profile considered in the analysis, the performance improves. Two laser projection schemes have been considered: central and lateral projection. In this framework, assuming for instance a WCoG algorithm and a reasonable detector noise RON = 3 e^-/pixel, it has been found that approximately $N_{ph} = 350-520$ (respectively referred to 270 - 200 nm) detected photons per subaperture per frame are required for the central laser projection. For comparison, the photon return of the Keck LGS system (Wizinowich et al., 2006), properly adapted to the case of the MCAO system for the E-ELT considering all relevant parameters, would correspond to approximately $N_{ph} \sim 70 - 180$; considering an average value of 125 detected photons per sub-aperture, the number of detected photons required to achieve our target WFE is a factor $\sim 2.5 - 4$ larger. In this context it is interesting to note that considering correlation or Quad-cell algorithm and detector noise RON = 3 e^-/pixel, the number of required photons per subaperture are $N_{ph} = 300 - 450$ and $N_{ph} = 210 - 330$ respectively. For the lateral laser projection, the required number of photons is about a factor ~ 2 or more larger than for the central projection. The choice between central and lateral projection depends not only on the number of required photons, but also on other aspects, e.g. contamination due to the Rayleigh scattering of the laser light in the lower atmosphere. A preliminary analysis of this effect in the case of central projection is reported in next Section.

A notable reduction in the required number of detected photons ($N_{ph} \simeq 210$, see Table 3.2 in Section 3.3.6) might be obtained canceling the perspective elongation by means of a dynamic refocus scheme (Angel, 2000) combined with

a pulsed laser, that is however more challenging from the technological point of view.

Other approaches have been investigated to achieve similar results without fast moving parts (see Section 3.4).

Algorithm	**Detected photons/subap (RON=3)**	**Detected photons/subap (RON=5)**	**pixel per subap**	**CCD size (pixels)**
WCoG	350-520	480-700	12×12	∼1K×1K
Correlation	300-450	370-520	12×12	∼1K×1K
Quad-cell	210-330	240-375	2×2	∼168×168

Table 4.1: Relevant quantities related to LGS SH WFS. LGS projected from behind M2. The two values of number of photons in each box are related to different assumptions on the closed loop filtering effect. The results are presented for Gaussian sodium profile.

A detailed analysis of the influence of the RON has been performed. Assuming a more conservative value RON = 5 e^-/pixel, the required number of detected photons increases by a factor ~ 1.4 with respect to the case RON = 3 e^-/pixel when the WCoG algorithm is considered. This factor is about 1.3 and 1.1 for correlation and Quad-cell respectively.

Another important aspect that has been analyzed is the number of pixels per subaperture, that determines the detector size. With typical Sodium profiles, assuming Nyquist sampling in the non elongated direction and central laser projection, the minimum number of pixels per subaperture is 12×12 for both the WCoG and the correlation, that for 84 subapertures across the diameter (Table 3.1) corresponds to a detector size of $\sim 1000 \times 1000$ pixels, that doubles in the case of lateral laser projection. This detector format, especially combined with a RON = 3 e^-/pixel or better looks a demanding requirement. In this sense, the adoption of a quad-cell scheme allows a dramatic reduction of the detector size (Table tab:doc2) although at the price of a larger sensitivity to calibration issues.

Additional aspects to be considered in the evaluation of the algorithms are the variation with time of the Sodium profile and the impact of the differential aberrations between science and LGS channel, that usually depend on the Zenithal angle variation during the exposure. The Sodium profile variations imply a continuous updating of the algorithm reference (the weighting function and the calibration curve in the case of the WCoG, the gain curve for the Quad-

cell algorithm); the differential aberrations may translate into time dependent spot offsets in the subapertures, that need to be compensated or calibrated. The evaluation of different algorithms, considering also these additional issues, is going to be analyzed with the support of a laboratory prototype, described in Section 4.3.

4.2 Very preliminary considerations on fratricide effect

The scope of this Section is to perform a preliminary analysis of the impact of the fratricide effect on the WFS noise propagation. The impact on the tomographic reconstructor and on other aspects is beyond the scope of this Thesis. As an exception in this Section, we will consider the several LGS channels involved, but to avoid complex tomographic reconstructors, we will still consider standard single channel reconstructors, in the sense that all LGSs measure the same signal.

Systems using multiple LGS beams with CW lasers are affected by fratricide effect, related to the Rayleigh scattering of the laser light in the lower atmosphere. A WFS looking at a LGS may collect the scattered light of other LGSs, causing a background increase in the subapertures. This is true when the LGSs are projected from behind the secondary mirror for instance, while in the case of edge launching the effect is not present. In this section the impact of this effect on the propagated WFE per LGS is discussed. To take into account this effect, the contribution of the Rayleigh background is translated into an increment of the equivalent RON in the affected subapertures. A pattern of the subapertures of a LGS WFS affected by fratricide effect is presented in Figure 4.1, showing the typical Rayleigh "plumes". The colored pixels in the picture represent the subapertures where the background noise associated to the scattering is $\geq 1\ e^-$; these subaperture signals have been simply discarded, in the described first order approach, to limit the Rayleigh induced noise excess; the "absolute" flux of the Rayleigh background was scaled to an LGS flux of 520 detected photons per subaperture, that corresponds to a request of 200 nm WFE (see Table 4.1). The noise pattern is rotated for different LGSs, therefore, in general, when the signals of different LGSs are "superimposed", there is no subaperture contaminated by all LGS signals simultaneously. After superimposition the scattering patterns of 6 LGSs can be described as follows: just few subapertures are strongly polluted having "only" 3 LGS channels

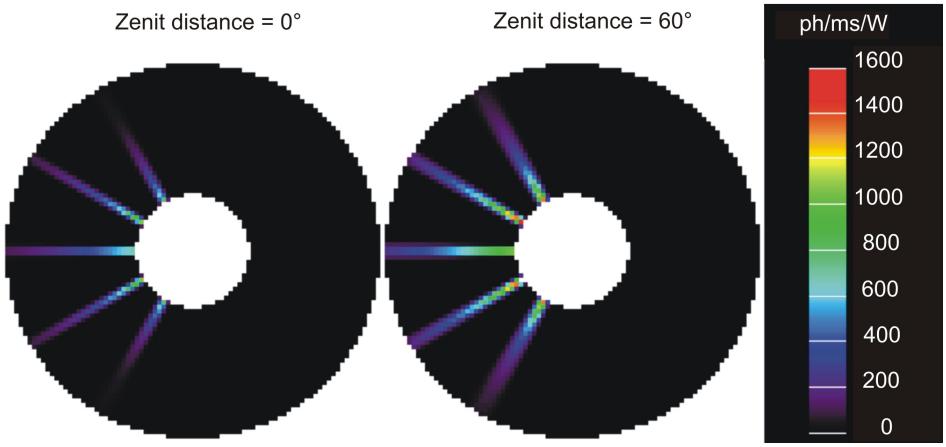

Figure 4.1: Subapertures affected by Rayleigh scattering in the pupil plane of one WFS looking at one LGS (colored pixels). The LGSs are launched at 2' FoV. (Courtesy of Enrico Marchetti, ESO).

satisfying our selection criterion (colored pixels in the figure). All the other subapertures receive a "usable" signal from at least 4 LGS (up to 6). In the subapertures with less than 6 usable signals, it may be assumed that the noise on the OPD measurement is higher. Taking this "extra-noise" into account, the OPD error per subaperture was propagated to WFE over the pupil, following the same approach presented in Chapter 3.

The impact of the fratricide effect was computed in the case of 520 detected photons per subaperture and 3 electrons RON for a Gaussian Sodium profile (see Table 4.1). The final WFE increases by $\sim$ 5 nm, from 200 nm to 205 nm. The test was also performed considering a higher flux per LGS, hence a higher level of Rayleigh background; the number of affected subapertures slightly increases, but a similar negligible increase in the final WFE is recorded. The conclusion that can be drawn from this preliminary analysis is that the fratricide effect has a negligible impact on the WFS noise propagation.

4.3 The laboratory prototype

Through a single channel analysis the effect of the spot elongation on the accuracy of spot position measurement with the SH WFS was numerically investigated in Chapter 3 and applied to the E-ELT case in Section 4.1. The two Sodium profiles used in the simulations were assumed to be constant in time (static), although the problem of the temporal variation of the Sodium

layer properties has to be addressed. In fact, even if all the three algorithms perform better than a simple center of gravity approach in the relevant conditions for the E-ELT MCAO module, however they all require some sort of 'reference'. The WCoG requires the knowledge of the average spot in each subaperture to compute a so-called weighting function; the correlation requires a spot template for the computation of the correlation function; the quad-cell approach requires the knowledge of the spot shape to calibrate the algorithm response. The complex and time variable change of the Sodium profile clearly represent a problem to be investigated in this respect. Another important aspect that has been addressed in the analysis is the impact of the low-order aberrations introduced on the LGS images by the MCAO module re-imaging optics for instance, that are optimized for infinite conjugate imaging, while the LGS is at a finite distance from the telescope. These low-order aberrations, that are also changing slowly with time, introduce what is called 'slope offset' in the subapertures. For relatively small offsets, this effect can be taken into account as a kind of bias in the measurements for certain algorithms (WCoG and correlation), but may compromise the performance of a quad-cell approach, where it should be compensated in some way. In any case, it is of primary importance to take into account this effect, for all types of algorithms. The scope of the LGS WFS laboratory prototype is to reproduce the relevant aspects of an LGS WFS Shack-Hartmann for the E-ELT and, through laboratory tests, evaluate the performance of different centroid algorithms in presence of elongated spots, with realistic Sodium profiles, as investigated numerically and analytically in Chapter 3, analyzing the impact of the low-order aberrations and of relevant WFS parameters, like SNR, sampling, subaperture size. The objectives of this activity are 1) the validation of the critical concepts that have been investigated so far only from the theoretical point of view and that are essential to guarantee the performance goals of the MCAO module, and 2) the acquisition of an experience that is crucial for the modeling, design and specification of the LGS WFS for the E-ELT. While the Shack-Hartmann WFS combined with advanced algorithms is the current baseline for the MCAO module, in the study framework other wavefront sensing concepts are being evaluated. One of these approaches is the modulated pyramid WFS. This concept is currently under investigation, to assess its requirements in terms of laser power. If the approach will turn out to

be competitive with the baseline Shack-Hartmann with advanced algorithms, the modulated pyramid might become an interesting alternative, that might dramatically relax the requirements on the detector format. The present layout of the LGS WFS prototype allows the duplication of the WFS module, introducing an additional WFS. This option, however, will be pursed only on a best effort basis and subject to the positive outcome of the theoretical analysis of the laser power requirements of such kind of WFS. The main components and the minimum requirements of the LGS WFS prototype that is the scope of this document are listed in the following:

- A light source able to reproduce the elongation pattern due to a LGS characterized by a realistic Sodium density profile. The minimum requirement on the elongation ratio q (i.e. ratio between elongated and non elongated spot axis) is $q > 3$ at the edge of the pupil.

- A pupil plane position to introduce phase screens to simulate, depending on the application, the atmospheric turbulence (in open or closed loop conditions) and/or the low-order aberrations that perturb the WFS measurements;

- A pupil plane with a lenslet array and a CCD in its focal plane to model the Shack Hartmann WFS. The number of sub-apertures is not critical but should be not far, at least as an order of magnitude, from the one assumed in the MCAO module design (40-50 sub-apertures across the diameter for instance);

- A pupil plane with a low-order deformable mirror able to reproduce low order aberrations affecting the WFS measurement or, depending on the application, able to compensate the low order aberrations introduced by the low order phase screen described before; the magnitude of these low order aberrations is related to the MCAO module optical design, but it should be in the range of $\sim 1\mu$m RMS.

4.3.1 Prototype design

This section briefly introduces the design concept of the lab-prototype to realize the conditions described in Section 4.3. A detailed description of the optical

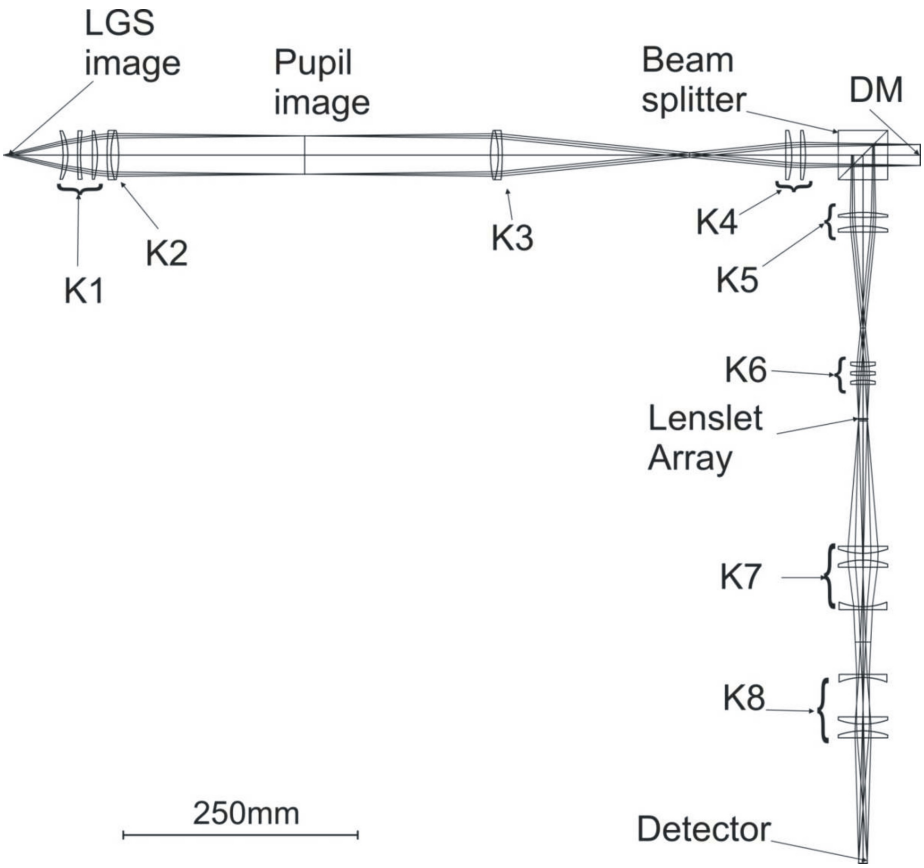

Figure 4.2: Optical design of the LGS WFS prototype. (Courtesy of Matteo Lombini, INAF, Osservatorio Astronomico di Bologna)

design of the prototype is beyond the scope of this thesis. The prototype can be separated in four modules:

- LGS source simulator that reproduce a realistic elongated LGS image with different density profiles;
- atmospheric turbulence simulator that introduces static wavefront aberrations by means of a phase screen or low order aberrations due to the MCAO module optics;
- low-order aberration simulator, represented by a DM positioned an intermediate pupil plane;
- the Shack-Hartmann WFS.

The optical design of the prototype is shown in Figure 4.2.

4.3.2 Test plan

A full set of planned tests is detailed in the following.

1. Evaluation of performance for a point source (no elongation) and comparison with analytical formulas and numerical simulations results.

2. Evaluation of performance in case of vertical extension of the source (elongated source) in four main cases, to be confirmed during the actual test phase: homogeneous emission along the extended source (non realistic 'rectangular' sodium profile); non homogeneous emission along the extended source in order to reproduce a realistic Gaussian Sodium profile; non homogeneous emission along the extended source in order to reproduce a bi-modal Sodium profile; non homogeneous emission along the extended source in order to reproduce one or more irregular Sodium profiles.

3. Evaluation of performance in different SNR conditions, e.g. bright case and faint case.

4. Evaluation of performance in the case of time variable source emission in order to emulate the variability of the Sodium density profile. The temporal aspect in itself is not crucial: the important aspect is the test of the algorithm performance on a given Sodium profile, using a reference (the weighting function for the WCoG) computed on a slightly different Sodium profile.

5. Evaluation of the effect of the slope offset due to the application of low order modes, simulating the LGS aberrations induced by the MCAO relay optics.

6. Evaluation of the algorithm with two different sampling. The prototype will be designed in order to give the possibility to change the pixel scale on the CCD changing the fiber diameter. The two available samplings will be $\sim$2 and $\sim$1.5 pixels per FWHM in the non-elongated direction.

7. As described in Chapter 3, windowing is essential to compute the position of spots with bimodal Sodium density profile. In fact

windowing allows to select only the sharper component of the spot, thus reducing the apparent elongation. The impact of different windows will be tested.

The rationale is to perform all the tests on the WCoG algorithm, that has been chosen as simple baseline in the MCAO system analysis presented in Section 4.1. Afterwards the alternative algorithms (likely correlation and quad-cell) are implemented and tested.

Conclusions

The Multi Conjugate Adaptive Optics technique plays a relevant role in the future of astrophysics research. The possibility to obtain the full potential in angular resolution over a wide FoV with telescopes having diameters up to 40 m, paves the way to the study of distant stellar populations and high redshift galaxies.

The capabilities of the MCAO technique was successfully proved on sky by means of the ESO MCAO Demonstrator (MAD) observing the Galactic globular cluster ω Centauri (Bono et al., 2009). In the star oriented configuration, MAD takes advantage of three natural guide stars for the atmospheric turbulence measurement. The author of the paper reporting the results of that observations, states in the abstract: '*The unprecedented quality of the images provided the opportunity to perform accurate photometry in the central crowded regions*'. This target was perfect for the intent to demonstrate the MCAO technique validity. In fact within a circle of ~ 1.5 arcmin around ω Cen there are three bright (~ 11 magnitude) Natural Guide Stars. How many targets in the sky can boast such a 'fortune'? The answer to this question defines the sky coverage, the fraction of the sky that contains sufficiently bright stars to achieve a given system performance. In the case of the star oriented approach an important parameter to establish the sky coverage is therefore the limiting magnitude of each guide star to obtain an accurate wavefront reconstruction.

In order to increase the sky coverage using only NGSs, the LBT MCAO system, NIRVANA, is based on the layer oriented approach. In a layer oriented system the WFSs are not coupled to a GS as for the star oriented approach, but they are conjugated with specific turbulent layers in the atmosphere. This technique permits to optically co-add the light from all the GSs in the FoV, thus reducing the impact of the RON. For this reason the limiting GS magnitude of the star oriented approach is replaced by the integrated magnitude over

the FoV. It is clear that increasing the number of GSs means to relax the single GS magnitude requirement. The upper limit of usable NGSs is fixed by the number of the GS probes used to collect the light from each star and to co-add this light on to a single detector. Even if this approach represents an interesting solution to increase the sky coverage using only NGSs, the opto-mechanical complexity of the overall system makes difficult the scaling to an ELT.

To ensure correction uniformity and a higher sky coverage, the baseline choice for the E-ELT MCAO system (MAORY) is the use of Sodium LGSs, artificial sources that can be created everywhere in the sky ideally solving the problem of lack of guide stars with the required characteristics. In point of fact the sky coverage is established by the need of few NGSs for the low-orders measurement that the LGSs cannot provide. Since the photon flux required from the NGSs is considerably less than that for high-order compensation, the impact on the sky coverage is not dramatic, even if definitely not negligible.

The use of LGSs in principle solves the problem of the lack of bright reference sources, but other difficulties arise. In particular in Chapter 3 the problem of the perspective elongation of the LGS image due to the non negligible thickness of the Sodium layer was discussed. When a SH WFS is implemented, a straightforward solution is to increase the laser power in order to compensate the loss of centroiding measurement accuracy due to the elongated shape of the spot. Moreover the WFS detector size required to re-image the elongated LGS images, combined with a low RON, is technologically challenging. Feasibility studies on more powerful and efficient laser systems and on big size / low noise detectors are in progress.

The implementation of a dynamic refocus scheme with a pulsed laser would represent an interesting alternative, but to avoid challenging and non available technologies, the research of an optical static solution was preferred. A new interesting WFS concept, not affected by the spot elongation, based only on already available technologies and really competitive in performance, was the result of this research: the bi-prisms WFS.

In addition to the spot elongation problem, also the variability of the Sodium layer (altitude and profile) and the aberrations introduced by the optics optimized for infinite conjugate imaging, have an impact on the performance of the WFS. In the immediate future these effects will be

investigated by means of a laboratory prototype, able to reproduce the most relevant aspects of an LGS Shack-Hartmann WFS for the E-ELT. The results of the numerical simulations and of the tests on the prototype will represent the starting point for the MAORY LGS WFS optical design.

Bibliography

Angel, J. R. P., 2000, Science with LBT, 21

Babcock, H. W., 1953, PASP, 65, 229

Beckers, J. M., 1989, in SPIE Proc., 1114, 215

Beckers J. M., 1993, Annu. Rev. Astron. Astrophys., 31, 13

Bono, G. et al, 2009, Science with the VLT in the ELT Era, 67

Conan, J.-M., Petit, C., Robert, C., Fusco, T., Neichel, B., Diolaiti, E., Foppiani, I., Schreiber, L., Esposito, S., Marchetti, E., 2008, Marseille Proc. SPIE 7015

Diolaiti E. et al., 2008, SPIE Proc., 7015, 70150U

Drummond J., Telle J., Denman C., Hillman P., Spinhirne J., Christou J., et al., 2004, PASP, 116, 952

Ellerbroek, B. L., & Rigaut, F. 2000, SPIE, 4007, 1088

Ellerbroek, B., L., Rigaut, F., J., Bauman, B. et al, 2003, Proc. SPIE 4839, 55-66

Foy R., Labeyrie A., 1985, A&A, 152, 129

Fugate R. Q., Fried D. L., Ameer G. A., Boeke B. R., Browne S. L., Roberts P. H., Ruane R. E., Tyler G. A., Wopat L. M., 1991, Nature, 353, 144

Fusco T., , 2004, SPIE Proc., 5490, 33

Georges J. A., Mallik P., Stalcup T., Angel J. R. P., Sarlot R., 2003, SPIE Proc., 4839, 473

Gilmozzi R., Spyromilio J., 2008, SPIE Proc., 7012, 701219

Hardy J. W., 1998, Adaptive optics for astronomical telescopes, Oxford University Press

T. M. Herbst et al., 2003, SPIE Conference Proceedings, 4838, 456

Herriot, G., Hickson, P., Ellerbroek, B., L., Andersen, D., et al , 2006, Proc. SPIE 6272, 62720Q

Hippler S., Hormuth F., Brandner W., Butler D. J., Henning T., Egner S., 2006, SPIE Conference Proceedings, Vol. 6272 627255-1

N. Hubin, E. Marchetti, R. Conan, R. Ragazzoni, E. Diolaiti, M. Tordi, G. Rousset, T. Fusco, P. Y. Madec, D. Butler, S. Esposito, 2002, ESO conference and Workshop Proceedings, 58 27–35

Kittmann F., et al., 2008, Proceedings SPIE Marseille

Lombini, M., Schreiber, L., Foppiani, I., Diolaiti, E., in preparation

Marchetti, E., Brast, R., Delabre, B. et al., 2006, SPIE 6272, 21

Nelson J. E., Sanders G. H., 2006, SPIE Proc., 6267, 2006

O'Sullivan, C., et Al., 2000, Experimental Astronomy, 10, 147

Ragazzoni, R., Farinato, J., & Marchetti, E., 2000, Spie, 4007, 1076

Ragazzoni, R., 1996, Journal of Modern Optics, 43, 289

Ragazzoni R., 1996, J. of Mod. Opt. 43, pp. 289-293

Ragazzoni, R. & Farinato, J., 1999, A&A, 350, L23

Ragazzoni, R., 1999, ESO Proc., 57, 175

Ragazzoni, R., Farinato, J., Marchetti, E., 2000, A&A, 136, 205

Ragazzoni R. et al., 2003, SPIE Conference Proceedings, 4839, 536.

Ragazzoni R., Diolaiti E., Farinato J., Fedrigo E., Marchetti E., Tordi M., Kirkman D., 2002, A&A 396, 731-744.

Rigaut, F., Gendron, E., 1992, A&A, 261, 677

Rigaut, F., et al., 1998, PASP, 110, 152

Rigaut, F., Ellerbroek, B. L., & Flicker, R., 2000, SPIE, 4007, 1022

Roddier, F., Northcott, M. J., Graves, J. E., McKenna, D. L., & Roddier, D., 1993, JOSA A, 10, 957

Roth, S., 2006, Diploma thesis.

Rousset G., 2004, in Adaptive optics in astronomy, ed. Roddier F., Cambridge University Press

Schreiber L. et al., 2009, accepted by MNRAS

Schreiber L., Lombini M., Foppiani I., Diolaiti E., Conan J.-M., Marchetti E., 2008, SPIE Proc., 7015, 70151O

Schreiber L. et al., 2008, SPIE Proc., 7015, 70155A

Simon, M., Close, L. M.,& Beck, T. L. 1999, AJ, 117, 1375

Thomas S., Fusco T., Tokovinin A., Nicolle M., Michau V., Rousset G., 2006, MNRAS, 371, 323

Thomas S., Adkins S., Gavel D., Fusco T., Michau V., 2008, MNRAS, 387, 173

Tyson R. K., 1998, Principles of Adaptive Optics, Academic Press

Viard, E. et al., 2000, Proc. SPIE, 4007, 94105

Wizinowich P. L. et al, 2006, PASP, 118, 297

http://www.eso.org/sci/facilities/eelt/instrumentation/index.html

Acknowledgements

I want to give a special thanks to Emiliano Diolaiti, Italo Foppiani and Matteo Lombini, for having taught me all what I know with patience and extreme competence.
I am grateful to Bruno Marano, for having put trust in me.
On the NIRVANA side, I thank Fulvio De Bonis, Daniel Meschke, Frank Kittmann, Peter Bizenberger, Wolfgang Gaessler, Lars Mohr, Sebastian Egner, Tom Herbst, Martin Kuerster, and the rest of the NIRVANA team.
I thank also Clelia Robert, Jean-Marc Conan (ONERA) and Enrico Marchetti (ESO) for the usefull discussions.
Thanks to my mum, Silvia, for the 'new invented-by-me matrix properties' support.
Thanks to Antonio, for his scientific and human support, I sincerely hope to enjoy his sweet company for a long long time.